

Three-dimensional stress analysis of structures in instability conditions using nonlinear displacement-based and hybrid-mixed quadrilaterals based on SaS formulation

Mehdi Bohlooly^{a,b}, G.M. Kulikov^{a,*}, S.V. Plotnikova^a, M.A. Kouchakzadeh^b

^a Laboratory of Intelligent Materials and Structures, Tambov State Technical University, Sovetskaya Street, 106, Tambov 392000, Russia

^b Department of Aerospace Engineering, Sharif University of Technology, Azadi Street, P.O. Box 11155-8639, Tehran, Iran

ARTICLE INFO

Keywords:

Displacement-based element
Hybrid-mixed element
SaS method
ANS method
Snapping conditions
Post-buckling

ABSTRACT

In this paper, the three-dimensional (3D) stress analysis of plate-type structures in instability conditions is presented. The displacement-based and hybrid-mixed four-node quadrilateral elements are developed taking the advantages of the sampling surfaces (SaS) method. The SaS formulation is based on considering inside the plate N not equally spaced SaS parallel to the middle surface to specify the displacements of these surfaces as primary plate unknowns. The displacements, strains and stresses are assumed to be distributed through the thickness using Lagrange polynomials of degree $N-1$ that lead to a well-set higher-order plate theory. The locations of SaS are based on the use of Chebyshev polynomial nodes that allow us to minimize uniformly the error due to Lagrange interpolation. To circumvent shear locking and have no spurious zero energy modes, the assumed transverse shear strains are employed. The nonlinear equilibrium equations are solved by the Newton-Raphson iterative method combined with the Crisfield arc-length algorithm. The accuracy and efficiency of both elements in different conditions such as coarse and distorted meshes are investigated. The developed assumed-natural strain (ANS) elements can be useful for the 3D stress analysis of thin and thick plates in whole states of equilibrium path involving bifurcation, snap-through, and/or snap-back phenomena.

1. Introduction

The analysis of structural mechanics has been hindered by the inherent complexity associated with the geometrically nonlinearities. The finite element formulation based on iterative methods is one of the most straightforward ways to analyze such nonlinear problems in large variety of situations. As a subcategory, structural stability exhibits a bifurcation or reduction of the load (snap-through) and/or displacements (snap-back). Such behaviors lead to more complexity whereby the load-control iterative method is not able to evaluate beyond the critical point (bifurcation and/or limit point).

Alternatively, a displacement-control method based on Newton-Raphson iterations solves singularity problems of tangential stiffness matrix and it is adequate to predict the bifurcation and snap-through points [1,2]. Nonetheless, this method cannot be applied for structural behavior including snap-back phenomenon. In addition, other strategies such as minimum residual displacement norm [3], generalized displacement-control [4], and energy-control [5,6] were proposed with different efficiency and robustness.

Structural stability analysis conducted by path-following technique (arc-length method) is a common method to trace beyond such critical

points. The crucial idea of this technique can be traced back to [7–9] where both load and displacement increments are unknown and the equilibrium equations can be solved by defining an additional arc-length equation. The path-following techniques are well established, many variants are proposed and their efficiency and robustness are evaluated [10–15]. Among these studies, a user friendly algorithm is presented by Crisfield [12] with widespread application in commercial finite element programs. In this paper, the Crisfield algorithm is applied to describe the bifurcation and snap-through phenomena through the higher-order SaS formulation, which is a natural extension of the 6-, 9- and 12-parameter models accounting for thickness stretching.

The simplest first-order theory accounting for thickness stretching is based on retaining two terms in power series with respect to the transverse coordinate for the displacements that leads to the 6-parameter model. This model has been widely used for developing the finite elements for plates and shells undergoing finite rotations and displacements [16–19]. However, because of thickness locking the 6-parameter model is unable to incorporate 3D constitutive laws. To prevent thickness locking, the constitutive equations can be modified by using the generalized plane stress conditions [16,18]. In order to utilize the 3D constitutive equations, the enhanced assumed strain

* Corresponding author.

E-mail address: gmkulikov@mail.ru (G.M. Kulikov).

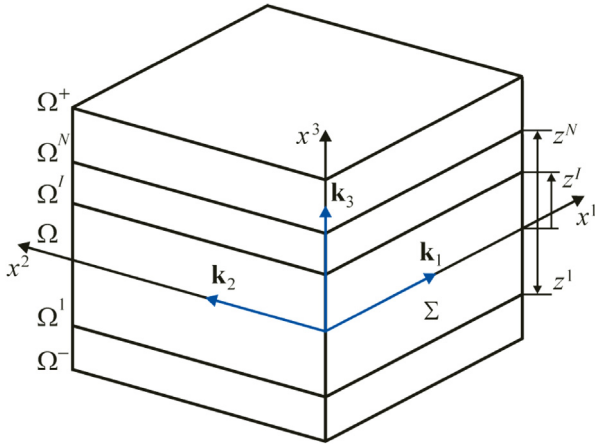


Fig. 1. Geometry of the plate.

method [17], in which the transverse normal strain is enriched in the thickness direction by a linear term, and the hybrid stress method [19], in which the transverse normal stress is assumed to be constant through the thickness, can be applied. The effective way of using the 3D constitutive equations is to employ the nonlinear 7-parameter model based on retaining additionally the third term in a power series for the transverse displacement. Such a model is optimal with respect to a number of degrees of freedom (DOF) and is very popular [20–26].

A more general 9-parameter model can be developed retaining three terms in power series for the in-plane and transverse displacements as described in [26–29]. The major drawback of the 9-parameter model is the inability to predict correctly the transverse components of the second Piola–Kirchhoff stress tensor as shown in contributions [26,27,29]. To solve the problem, more general 12- and 15-parameter models were proposed [27,29–31]. In particular, Pagani et al. [29] established the importance of using full Green–Lagrange strain–displacement equations for the post-buckling analysis of rectangular plates. However, to the authors’ best knowledge, no results are available in the literature regarding the accurate prediction of *all* components of the second Piola–Kirchhoff stress tensor in plate structures in instability conditions. Moreover, in available finite element formulations based on the higher-order models, only rectangular elements are utilized that are far from technical applications.

The effective way of constructing general higher-order models is to use the SaS method [32,33]. The SaS method is based on choosing inside the plate N SaS parallel to the middle surface, in order to introduce the displacements of these surfaces as basic plate unknowns, where $N \geq 3$. Such choice of unknowns with the use of Lagrange polynomials of degree $N-1$ in the through-thickness distributions of displacements, strains and stresses yields a robust higher-order shell formulation. Thus, we deal here with a $3N$ -parameter model, in particular, with 9-, 12- and 15-parameter models in the case of choosing three, four and five SaS inside the plate body and so on. In fact, there are no restrictions on the development of general higher-order models of arbitrary orders.

The location of SaS plays an important role into a SaS formulation, since the choice of equally spaced SaS can lead to divergence in the case of using the Lagrange polynomials of high degree as a number of SaS tends to infinity. However, choosing the locations based on Chebyshev polynomial nodes makes it possible to uniformly minimize the error due to Lagrange interpolation [34]. Recently, the SaS formulation was applied for the 3D nonlinear stress analysis of isotropic and composite structures through geometrically exact four-node rectangular solid-shell elements [35,36]. Here, more general four-node quadrilateral elements with particular attention to snapping and buckling problems are developed.

Due to robustness and simplicity, the isoparametric low-order elements have prevalent application. A main challenge of these elements

is shear locking, which occurs in bending dominated problems. To avoid shear locking and have no spurious zero energy modes, the assumed natural strain (ANS) method [37,38] can be applied. The ANS interpolation suppresses parasitic transverse shear strains considering pure bending deformations. Note that the ANS method has been already used to develop the geometrically linear SaS plate quadrilaterals [39]. To improve the computational efficiency of nonlinear ANS plate elements, a hybrid-mixed method can be applied [40, 41]. This method is based on using the Hellinger–Reissner variational principle, in which the displacements and stresses are utilized as independent variables. The advantages of the hybrid-mixed elements over widespread displacement-based elements have been established in many works [16,18,19,24,26,35]. Here, these results are confirmed for SaS plate quadrilaterals.

The aim of this paper is to develop a 3D stress analysis of plate-type structures in instability conditions. For such purpose, the displacement-based and hybrid-mixed four-node quadrilateral elements using the ANS method and the SaS method are proposed. The resulting equilibrium equations are solved by a Crisfield arc-length algorithm incorporated into a Newton–Raphson method. This makes it possible to conclude that the presented 3D stress analysis of plate structures in instability conditions is a significant contribution to solid mechanics, since both developed SaS plate quadrilaterals allow us to calculate all components of the second Piola–Kirchhoff stress tensor in entire states of equilibrium path such as pre-buckling range, buckling point and post-buckling range.

2. Displacement-based ANS quadrilateral plate element

Consider a plate-type structure of the thickness h . The plate can be described as a 3D body of volume V , which is bounded by top, bottom and edge surfaces Ω^+ , Ω^- and Σ , respectively. The origin of a Cartesian coordinate system (x^1, x^2, x^3) is located on the mid-surface Ω such that the coordinate x^3 is oriented along the thickness as illustrated in Fig. 1. Introduce inside the plate N not equally spaced SaS parallel to the middle surface to accept the displacements of these surfaces as basic plate unknowns. The transverse coordinates of SaS Ω^I ($I = 1, 2, \dots, N$) are given by

$$z^I = -\frac{h}{2} \cos\left(\pi \frac{2I-1}{2N}\right). \quad (1)$$

Herein, the locations of SaS coincide with the coordinates of the Chebyshev polynomial nodes (the roots of the Chebyshev polynomial of degree N). These locations lead to better convergence characteristics of the SaS method [32,33].

In order to perform the approximation for displacement distributions through the thickness, we introduce the first fundamental assumption of the SaS plate formulation [39] as follows:

$$u_i = \sum_I L^I u_i^I, \quad u_i^I = u_i(z^I), \quad (2)$$

where $u_i^I(x^1, x^2)$ are the displacements of SaS; $L^I(x^3)$ are the Lagrange basis polynomials of degree $N-1$ defined as

$$L^I = \prod_{J \neq I} \frac{x^3 - z^J}{z^I - z^J}, \quad J = 1, 2, \dots, N. \quad (3)$$

The following step consists in the choice of the consistent approximation for strains through the thickness of the plate. It is apparent that the strain distribution should be chosen similar to the displacement distribution in Eq. (2):

$$\varepsilon_{ij} = \sum_I L^I \varepsilon_{ij}^I, \quad \varepsilon_{ij}^I = \varepsilon_{ij}(z^I), \quad (4)$$

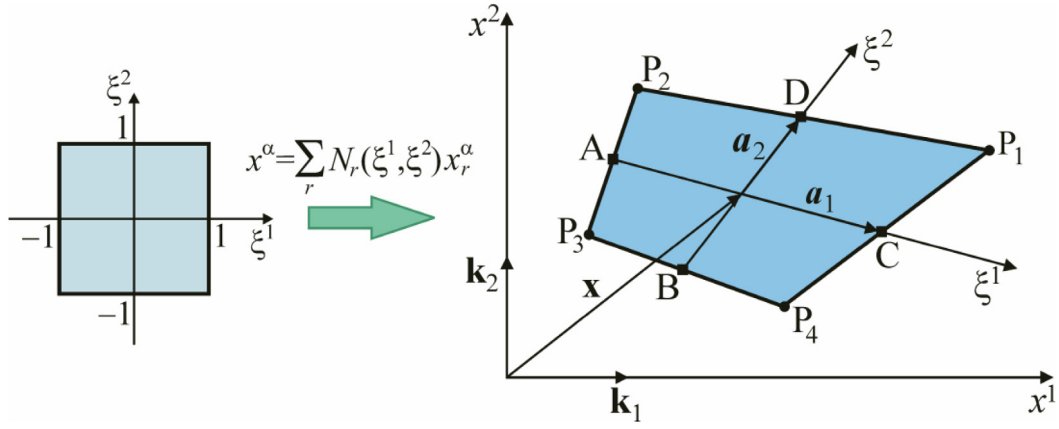


Fig. 2. Quadrilateral plate element.

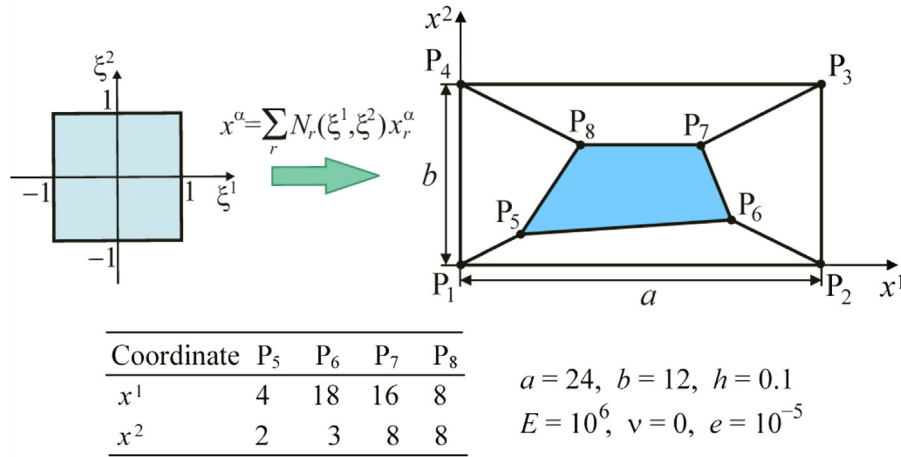


Fig. 3. Plate patch test.

where $\epsilon_{ij}^I(x^1, x^2)$ are the components of the Green–Lagrange strain tensor of SaS [35] given by

$$2\epsilon_{\alpha\beta}^I = \lambda_{\alpha\beta}^I + \lambda_{\beta\alpha}^I + \sum_i \lambda_{i\alpha}^I \lambda_{i\beta}^I,$$

$$2\epsilon_{\alpha 3}^I = \beta_\alpha^I + \lambda_{3\alpha}^I + \sum_i \lambda_{i\alpha}^I \beta_i^I,$$

$$2\epsilon_{33}^I = 2\beta_3^I + \sum_i \beta_i^I \beta_i^I,$$

(5)

and

$$\lambda_{i\alpha}^I = u_{i,\alpha}^I, \quad \beta_i^I = \sum_J M^J(x_3^I) u_i^J,$$

(6)

where $M^I = L_3^I$ are the polynomials of degree $N - 2$; their values on SaS are

$$M^J(z^I) = \frac{1}{z^J - z^I} \prod_{K \neq I, J} \frac{z^I - z^K}{z^J - z^K} \text{ for } J \neq I,$$

$$M^I(z^I) = - \sum_{J \neq I} M^J(z^I).$$

(7)

Here, Latin indices i, j range from 1 to 3; Greek indices α, β range from 1 to 2; and the symbol $(\dots)_i$ stands for the partial derivatives with respect to coordinates x^i .

According to constitutive equations, the following stress distribution can be derived similar to the strain distribution in Eq. (4):

$$S_{ij} = \sum_I L^I S_{ij}^I, \quad S_{ij}^I = S_{ij}(z^I),$$

(8)

where $S_{ij}^I(x^1, x^2)$ are the components of the second Piola–Kirchhoff stress tensor of SaS defined as

$$S_{ij}^I = \sum_k \sum_l C_{ijkl} \epsilon_{kl}^I, \quad k, l = 1, 2, 3$$

(9)

and C_{ijkl} are the elastic constants of the material.

By applying through-thickness distributions (2), (4) and (8) into the principle of virtual work and introducing the weighted coefficients

$$A^{IJ} = \int_{-h/2}^{h/2} L^I L^J dx^3,$$

(10)

the following variational equation in terms of SaS variables is obtained

$$\iint_{\Omega} \sum_I \sum_J A^{IJ} \delta(\epsilon^I)^T C \epsilon^J dx^1 dx^2 = \delta W,$$

(11)

$$W = \iint_{\Omega} ((\mathbf{u}^+)^T \mathbf{p}^+ - (\mathbf{u}^-)^T \mathbf{p}^-) dx^1 dx^2 + W_{\Sigma},$$

(12)

where

$$\epsilon^I = [\epsilon_{11}^I \quad \epsilon_{22}^I \quad \epsilon_{33}^I \quad 2\epsilon_{12}^I \quad 2\epsilon_{13}^I \quad 2\epsilon_{23}^I]^T,$$

$$\mathbf{u}^+ = [u_1^+ \quad u_2^+ \quad u_3^+]^T, \quad \mathbf{u}^- = [u_1^- \quad u_2^- \quad u_3^-]^T,$$

$$\mathbf{p}^+ = [p_1^+ \quad p_2^+ \quad p_3^+]^T, \quad \mathbf{p}^- = [p_1^- \quad p_2^- \quad p_3^-]^T,$$

$$C = \begin{bmatrix} C_{1111} & C_{1122} & C_{1133} & C_{1112} & 0 & 0 \\ C_{2211} & C_{2222} & C_{2233} & C_{2212} & 0 & 0 \\ C_{3311} & C_{3322} & C_{3333} & C_{3312} & 0 & 0 \\ C_{1211} & C_{1222} & C_{1233} & C_{1212} & 0 & 0 \\ 0 & 0 & 0 & 0 & C_{1313} & C_{1323} \\ 0 & 0 & 0 & 0 & C_{2313} & C_{2323} \end{bmatrix},$$

(13)

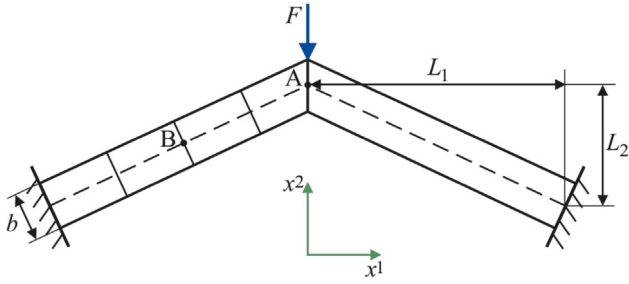


Fig. 4. Half of the toggle frame modeled by 4×1 mesh.

where u_i^+ and u_i^- are the displacements of top and bottom surfaces Ω^+ and Ω^- ; p_i^+ and p_i^- are the tractions on top and bottom surfaces; W_Σ is the work done by external loads applied to the edge surface Σ .

A simple finite element interpolation through SaS four-node plate quadrilaterals [39] can be written as

$$x^\alpha = \sum_r N_r x_r^\alpha, \quad (14)$$

$$u_i^l = \sum_r N_r u_{ir}^l, \quad (15)$$

$$N_r = \frac{1}{4} (1 + n_{1r} \xi^1) (1 + n_{2r} \xi^2), \quad (16)$$

$$n_{1r} = \begin{cases} 1 & \text{for } r = 1, 4 \\ -1 & \text{for } r = 2, 3 \end{cases}, \quad n_{2r} = \begin{cases} 1 & \text{for } r = 1, 2 \\ -1 & \text{for } r = 3, 4 \end{cases},$$

where $N_r(\xi^1, \xi^2)$ are the bilinear shape functions of the element; x_r^α are the nodal coordinates; u_{ir}^l are the displacements of SaS at element nodes; and the index r denotes the number of nodes ranging from 1 to 4. The standards of local numbering of the nodes are shown in Fig. 2.

To overcome shear locking and avoiding spurious zero energy modes, we apply the reliable ANS interpolation [37,38] of the transverse shear strains of SaS [39] with four sampling points A, B, C, and D, shown in Fig. 2,

$$\varepsilon_{\alpha 3}^l = \ell_{\alpha}^l \varepsilon_{13}^l + \ell_{\alpha}^l \varepsilon_{23}^l, \quad (17)$$

and

$$\varepsilon_{13}^l = \frac{1}{2} (1 - \xi_2) \varepsilon_{13}^l(B) + \frac{1}{2} (1 + \xi_2) \varepsilon_{13}^l(D), \quad (18)$$

$$\varepsilon_{23}^l = \frac{1}{2} (1 - \xi_1) \varepsilon_{23}^l(A) + \frac{1}{2} (1 + \xi_1) \varepsilon_{23}^l(C),$$

where $\varepsilon_{\alpha 3}^l$ are the covariant components of the Green–Lagrange strain tensor of SaS in the contravariant basis a^i defined as $a_i \cdot a^j = \delta_i^j$; and ℓ_{α}^l are the elements of the inverse Jacobian matrix given in Appendix A.

By introducing the displacement vector of the plate element

$$\mathbf{q} = [\mathbf{q}_1^T \ \mathbf{q}_2^T \ \mathbf{q}_3^T \ \mathbf{q}_4^T]^T, \quad (19)$$

$$\mathbf{q}_r = [u_{1r}^1 \ u_{2r}^1 \ u_{3r}^1 \ u_{1r}^2 \ u_{2r}^2 \ u_{3r}^2 \ \dots \ u_{1r}^N \ u_{2r}^N \ u_{3r}^N]^T,$$

and applying Eqs. (5), (6) and (15)–(18), the nonlinear nodal strain–displacement equations are written as

$$\varepsilon^l = \mathbf{B}^l \mathbf{q} + \mathbf{A}^l(\mathbf{q}) \mathbf{q}, \quad (20)$$

where \mathbf{B}^l and $\mathbf{A}^l(\mathbf{q})$ are linear and nonlinear matrices of order $6 \times 12N$. The definition of $\mathbf{A}^l(\mathbf{q})$ is expressed as

$$\mathbf{A}^l(\mathbf{q}) = \begin{bmatrix} \mathbf{q}^T \Pi_1^l \\ \mathbf{q}^T \Pi_2^l \\ \mathbf{q}^T \Pi_3^l \\ \mathbf{q}^T \Pi_4^l \\ \mathbf{q}^T \Pi_5^l \\ \mathbf{q}^T \Pi_6^l \end{bmatrix}, \quad (\mathbf{A}^l(\mathbf{q}))^T = [\Pi_1^l \mathbf{q} \ \Pi_2^l \mathbf{q} \ \Pi_3^l \mathbf{q} \ \Pi_4^l \mathbf{q} \ \Pi_5^l \mathbf{q} \ \Pi_6^l \mathbf{q}], \quad (21)$$

where $\Pi_s^l (s = 1, 2, \dots, 6)$ are the symmetric matrices of order $12N \times 12N$ defined in Appendix A.

Substituting (14), (15) and (20) in Eqs. (11) and (12), and taking into account that

$$\delta \varepsilon^l = (\mathbf{B}^l + 2\mathbf{A}^l(\mathbf{q})) \delta \mathbf{q}, \quad (22)$$

the nonlinear equilibrium equations of the ANS quadrilateral plate element are obtained

$$\mathbf{K}_S(\mathbf{q}) \mathbf{q} = \mathbf{F}, \quad (23)$$

where the secant stiffness matrix $\mathbf{K}_S(\mathbf{q})$ is defined as

$$\mathbf{K}_S(\mathbf{q}) = \sum_I \sum_J \Lambda^{IJ} \int_{-1}^1 \int_{-1}^1 (\mathbf{B}^l + 2\mathbf{A}^l(\mathbf{q}))^T \times \mathbf{C} (\mathbf{B}^l + \mathbf{A}^l(\mathbf{q})) \det(\mathbf{J}) d\xi^1 d\xi^2. \quad (24)$$

By implementing the incremental procedure to generate new state $({}^{t+\Delta t} \mathbf{q}, {}^{t+\Delta t} \mathbf{F})$ from known state $({}^t \mathbf{q}, {}^t \mathbf{F})$:

$${}^{t+\Delta t} \mathbf{q} = {}^t \mathbf{q} + \Delta \mathbf{q}, \quad {}^{t+\Delta t} \mathbf{F} = {}^t \mathbf{F} + \Delta \mathbf{F}, \quad (25)$$

which yields

$$\mathbf{K}_S({}^t \mathbf{q} + \Delta \mathbf{q}) ({}^t \mathbf{q} + \Delta \mathbf{q}) = {}^t \mathbf{F} + \Delta \mathbf{F}, \quad (26)$$

or

$$\mathbf{K}_S({}^t \mathbf{q}) \Delta \mathbf{q} + \mathbf{K}_N(\Delta \mathbf{q}) ({}^t \mathbf{q} + \Delta \mathbf{q}) = \Delta \mathbf{F}, \quad (27)$$

where

$$\mathbf{K}_N(\Delta \mathbf{q}) = \sum_I \sum_J \Lambda^{IJ} \int_{-1}^1 \int_{-1}^1 [(\mathbf{B}^l + 2\mathbf{A}^l({}^t \mathbf{q}))^T \mathbf{C} \mathbf{A}^l(\Delta \mathbf{q}) + 2(\mathbf{A}^l(\Delta \mathbf{q}))^T \mathbf{C} (\mathbf{B}^l + \mathbf{A}^l({}^t \mathbf{q} + \Delta \mathbf{q}))] \det(\mathbf{J}) d\xi^1 d\xi^2. \quad (28)$$

Unlike the load-control Newton–Raphson method, which $\Delta \mathbf{q}$ is the only unknown vector, here both parameters $(\Delta \mathbf{q}, \Delta \mathbf{F})$ are unknown. In order to simplify above equation, the expression $\Delta \mathbf{F} = \Delta \varphi \bar{\mathbf{F}}$ is defined, which means the load vector change by scalar parameter $\Delta \varphi$ during loading. Thus, the remaining unknowns are $(\Delta \mathbf{q}, \Delta \varphi)$ and Eq. (27) leads to

$$\mathbf{K}_S({}^t \mathbf{q}) \Delta \mathbf{q} + \mathbf{K}_N(\Delta \mathbf{q}) ({}^t \mathbf{q} + \Delta \mathbf{q}) = \Delta \varphi \bar{\mathbf{F}}. \quad (29)$$

Due to non-linear terms in incremental equation (29), the Newton–Raphson iteration process should be employed

$$\Delta \mathbf{q}^{[n+1]} = \Delta \mathbf{q}^{[n]} + \Delta \tilde{\mathbf{q}}^{[n]}, \quad (30)$$

$$\Delta \varphi^{[n+1]} = \Delta \varphi^{[n]} + \Delta \tilde{\varphi}^{[n]},$$

$n = 0, 1, \dots, \text{NIter}$,

where NIter is the number of iterations. As a result, the linearized equilibrium equations are written as

$$\mathbf{K}_T \Delta \tilde{\mathbf{q}}^{[n]} = \Delta \mathbf{F}^{[n]} + \Delta \tilde{\varphi}^{[n]} \bar{\mathbf{F}}, \quad (31)$$

where $\mathbf{K}_T = \mathbf{K}_D + \mathbf{K}_H$ is the tangent stiffness matrix of order $12N \times 12N$; $\Delta \mathbf{F}^{[n]}$ is the right-hand side vector given by

$$\mathbf{K}_D = \sum_I \sum_J \Lambda^{IJ} \int_{-1}^1 \int_{-1}^1 (\mathbf{L}^l ({}^t \mathbf{q} + \Delta \mathbf{q}^{[n]}))^T \times \mathbf{C} \mathbf{L}^l ({}^t \mathbf{q} + \Delta \mathbf{q}^{[n]}) \det(\mathbf{J}) d\xi^1 d\xi^2, \quad (32)$$

$$\mathbf{K}_H = 2 \sum_I \sum_J \Lambda^{IJ} \int_{-1}^1 \int_{-1}^1 \mathbf{H}^l [\mathbf{C} (\mathbf{B}^l + \mathbf{A}^l ({}^t \mathbf{q} + \Delta \mathbf{q}^{[n]})) ({}^t \mathbf{q} + \Delta \mathbf{q}^{[n]})] \times \det(\mathbf{J}) d\xi^1 d\xi^2, \quad (33)$$

$$\Delta \mathbf{F}^{[n]} = \Delta \varphi^{[n]} \bar{\mathbf{F}} - \sum_I \sum_J \Lambda^{IJ} \int_{-1}^1 \int_{-1}^1 \{ (\mathbf{L}^l ({}^t \mathbf{q} + \Delta \mathbf{q}^{[n]}))^T \times \mathbf{C} (\mathbf{L}^l ({}^t \mathbf{q} + \Delta \mathbf{q}^{[n]}) - \mathbf{A}^l(\Delta \mathbf{q}^{[n]})) + 2\mathbf{H}^l [\mathbf{C} (\mathbf{B}^l + \mathbf{A}^l ({}^t \mathbf{q})) ({}^t \mathbf{q})] \} \Delta \mathbf{q}^{[n]} \det(\mathbf{J}) d\xi^1 d\xi^2, \quad (34)$$

where

$$\mathbf{L}^l(\mathbf{q}) = \mathbf{B}^l + 2\mathbf{A}^l(\mathbf{q}). \quad (35)$$

Table 1
Convergence study for William's toggle frame with three SaS.

Element	Mesh	$\Delta \ell$	Upper critical load			Lower critical load		
			F	$-\bar{u}_2$ (A)	NStat/NIter	F	$-\bar{u}_2$ (A)	NStat/NIter
SaSD4	4×1	1×10^{-2}	–	–	failed	–	–	failed
	8×1	1.5×10^{-2}	–	–	failed	–	–	failed
	16×1	2×10^{-2}	–	–	failed	–	–	failed
	32×1	2.5×10^{-2}	–	–	failed	–	–	failed
	64×1	3×10^{-2}	–	–	failed	–	–	failed
	128×1	3.5×10^{-2}	36.00	0.248	122/280	34.67	0.375	184/426
SaSH4	256×1	4×10^{-2}	34.35	0.236	143/314	32.10	0.387	234/517
	4×1	1×10^{-2}	37.19	0.257	90/178	35.40	0.399	139/276
	8×1	1.5×10^{-2}	34.58	0.236	73/182	32.07	0.396	122/309
	16×1	2×10^{-2}	33.99	0.234	74/189	31.36	0.394	124/324
	32×1	2.5×10^{-2}	33.84	0.231	81/206	31.18	0.392	137/355
	64×1	3×10^{-2}	33.80	0.232	95/236	31.14	0.393	160/405
	128×1	3.5×10^{-2}	33.79	0.232	114/272	31.12	0.392	192/464
	256×1	4×10^{-2}	33.78	0.231	140/311	31.11	0.392	237/532

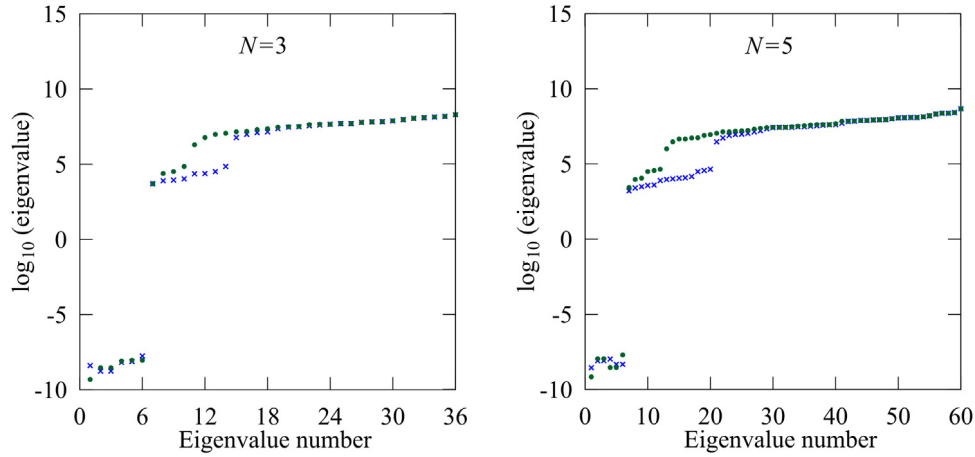


Fig. 5. Eigenvalues of half of the toggle frame with three and five SaS using SaSD4 (●) and SaSH4 (×) elements.

The equilibrium equations (31) for each element can be assembled by a standard technique to form the global equilibrium equations as follows:

$$\mathbf{K}_T^G \Delta \tilde{\mathbf{U}}^{[n]} = \Delta \mathbf{F}^{G[n]} + \Delta \tilde{\varphi}^{[n]} \bar{\mathbf{F}}^G, \quad (36)$$

where \mathbf{K}_T^G , $\Delta \tilde{\mathbf{U}}^{[n]}$, $\Delta \mathbf{F}^{G[n]}$, and $\bar{\mathbf{F}}^G$ denote the global form of \mathbf{K}_T , $\Delta \tilde{\mathbf{q}}^{[n]}$, $\Delta \mathbf{F}^{[n]}$, and $\bar{\mathbf{F}}$, respectively.

In order to implement the arc-length method, based on the Riks formulation [9], into the Newton–Raphson method, the following equation should be applied

$$(\Delta \mathbf{U}^{[n]} + \Delta \tilde{\mathbf{U}}^{[n]})^T \cdot (\Delta \mathbf{U}^{[n]} + \Delta \tilde{\mathbf{U}}^{[n]}) + \psi^2 (\Delta \varphi^{[n]} + \Delta \tilde{\varphi}^{[n]})^2 ((\bar{\mathbf{F}}^G)^T \cdot \bar{\mathbf{F}}^G) = \Delta \ell^2, \quad (37)$$

where the parameter $\Delta \ell$ denotes a prescribed distance to search for the next state. The parameter ψ describes a hyper ellipse surface in finding next equilibrium point. In the simple case, one can consider $\psi = 0$. It leads to a cylindrical arc-length method [12]. By eliminating incremental displacement $\Delta \tilde{\mathbf{U}}^{[n]}$ from Eqs. (36) and (37), a quadratic equation can be calculated as follows

$$\zeta_2^{[n]} (\Delta \tilde{\varphi}^{[n]})^2 + \zeta_1^{[n]} \Delta \tilde{\varphi}^{[n]} + \zeta_0^{[n]} = 0, \quad (38)$$

where the coefficients $\zeta_2^{[n]}$, $\zeta_1^{[n]}$ and $\zeta_0^{[n]}$ may be derived as

$$\begin{aligned} \zeta_2^{[n]} &= ((\mathbf{K}_T^G)^{-1} \bar{\mathbf{F}}^G)^T ((\mathbf{K}_T^G)^{-1} \bar{\mathbf{F}}^G), \\ \zeta_1^{[n]} &= 2((\mathbf{K}_T^G)^{-1} \bar{\mathbf{F}}^G)^T ((\mathbf{K}_T^G)^{-1} \Delta \mathbf{F}^{G[n]} + \Delta \mathbf{U}^{[n]}), \\ \zeta_0^{[n]} &= -\Delta \ell^2 + ((\mathbf{K}_T^G)^{-1} \Delta \mathbf{F}^{G[n]} + \Delta \mathbf{U}^{[n]})^T ((\mathbf{K}_T^G)^{-1} \Delta \mathbf{F}^{G[n]} + \Delta \mathbf{U}^{[n]}). \end{aligned} \quad (39)$$

Remark 1. As expected, the tangent stiffness matrix \mathbf{K}_T is symmetric. This is due to the symmetry of matrices \mathbf{K}_D and \mathbf{K}_H . The symmetry

of the latter matrix follows directly from the symmetry of matrices \mathbf{H}^I according to Proposition 1 in Appendix B.

Remark 2. To calculate the weighted coefficients A^{IJ} from Eq. (10), the N -point Gaussian quadrature rule in order to fulfill exact integration are utilized. This is sufficient because L^I are the Lagrange basis polynomials of degree $N - 1$.

Remark 3. The equilibrium equation (36) should be performed until the required accuracy of the solution

$$\|\Delta \mathbf{U}^{[n+1]} - \Delta \mathbf{U}^{[n]}\| < \varepsilon \|\Delta \mathbf{U}^{[n]}\| \quad (40)$$

is reached, where $\|\dots\|$ stands for the Euclidean norm; $\Delta \mathbf{U}$ is the global vector of displacement increments; ε is the prescribed tolerance.

Remark 4. Calculating Eq. (38) leads to two different solutions ($\Delta \tilde{\varphi}_1^{[n]}$, $\Delta \tilde{\varphi}_2^{[n]}$) and corresponding displacement vectors ($\Delta \mathbf{U}_1^{[n+1]}$, $\Delta \mathbf{U}_2^{[n+1]}$). To avoid move back phenomenon (so-called track-back), it is important to select the proper solution [12]. It can be determined by the smallest angle or, equivalently, the largest value of the following dot products:

$$\begin{aligned} \theta_1^{[n+1]} &= (\Delta \mathbf{U}^{[n]})^T \cdot \Delta \mathbf{U}_1^{[n+1]} \\ \theta_2^{[n+1]} &= (\Delta \mathbf{U}^{[n]})^T \cdot \Delta \mathbf{U}_2^{[n+1]}. \end{aligned} \quad (41)$$

At the beginning of each iteration process ($n = 0$), the global displacement vector is zero ($\Delta \mathbf{U}^{[0]} = 0$). Therefore, both ($\theta_1^{[1]}$, $\theta_2^{[1]}$) will be equal to zero, that is, the proper solution between ($\Delta \tilde{\varphi}_1^{[n]}$, $\Delta \tilde{\varphi}_2^{[n]}$) is the one with similar sign as the determinant of tangent stiffness matrix. In addition, there are other criteria, which choose a proper solution at the first iteration [42].

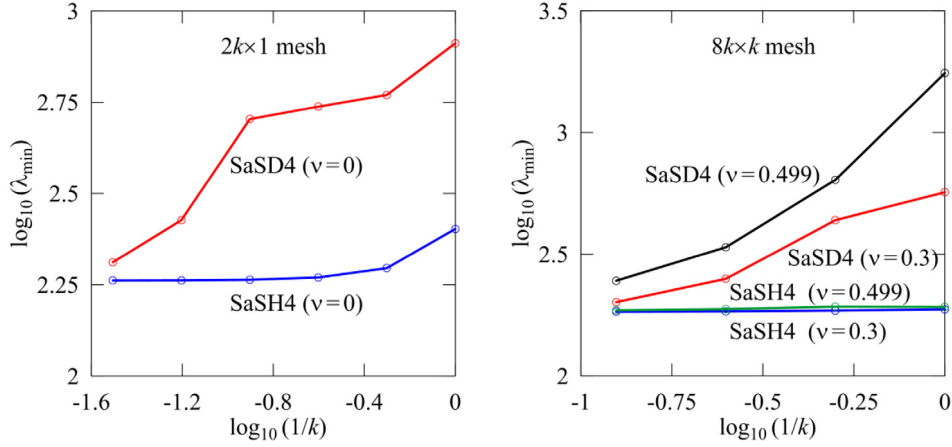


Fig. 6. Convergence of the smallest nonzero eigenvalue for different Poisson's ratios using three SaS and distorted meshes $2k \times 1$ and $8k \times k$, where $k = 1, 2, 4, 8, 16$ and 32 .

Table 2
Critical load of the column with $e = -h/10^4$ using three SaS and $\Delta \ell = 10^{-3}$.

Element	Mesh	$10^3 \times F$
SaSD4	4×1	0.2524
	8×1	0.2475
	16×1	0.2463
	32×1	0.2460
	64×1	0.2460
SaSH4	4×1	0.2524
	8×1	0.2475
	16×1	0.2463
	32×1	0.2460
Timoshenko and Gere [43]	-	0.2460

Table 3
Results for the column with $e = -h/2$ using three SaS, 32×1 mesh and $N_{Stat} = 1$.

Element	$\Delta \ell$	10	100	400	800	1000
SaSD4	NIter	5	8	17	24	33
	$10^4 \times F$	1.7353	2.3839	2.7431	4.2966	7.0790
	$-\bar{u}_3(A)$	1.4918	14.620	54.310	80.634	72.270
SaSH4	NIter	4	6	6	13	17
	$10^4 \times F$	1.7353	2.3839	2.7431	4.2955	7.0789
	$-\bar{u}_3(A)$	1.4918	14.620	54.310	80.633	72.270

3. Hybrid-mixed ANS quadrilateral plate element

In order to introduce the SaS quadrilateral plate element with a higher computational efficiency with respect to the previous nonlinear displacement-based ANS quadrilateral, the hybrid-mixed method can be applied [19,26,35]. By using through-thickness distributions (2), (4) and (8) into a Hellinger–Reissner variational principle [40], the variational equation consisting of SaS variables can be expressed as

$$\iint_{\Omega} \sum_I \sum_J A^{IJ} \left[\delta(S^I)^T (\epsilon^J - C^{-1}S^J) + \delta(\epsilon^I)^T S^J \right] dx^1 dx^2 = \delta W, \quad (42)$$

where

$$S^I = [S_{11}^I \ S_{22}^I \ S_{33}^I \ S_{12}^I \ S_{13}^I \ S_{23}^I]^T. \quad (43)$$

To fulfill a patch test, the stresses of SaS are interpolated throughout the element as suggested by Kulikov and Plotnikova [39]:

$$S^I = P\Phi^I, \quad (44)$$

where

$$\Phi^I = [\Phi_1^I \ \Phi_2^I \ \dots \ \Phi_{12}^I]^T, \quad (45)$$

$$P = \begin{bmatrix} 1 & 0 & 0 & 0 & 0 & 0 & \bar{t}_1^{-1} \bar{t}_1^{-2} \bar{\xi}^{-2} & \bar{t}_2^{-1} \bar{t}_2^{-1} \bar{\xi}^{-1} & 0 & 0 & 0 & 0 \\ 0 & 1 & 0 & 0 & 0 & 0 & \bar{t}_1^{-2} \bar{t}_1^{-2} \bar{\xi}^{-2} & \bar{t}_2^{-2} \bar{t}_2^{-2} \bar{\xi}^{-1} & 0 & 0 & 0 & 0 \\ 0 & 0 & 1 & 0 & 0 & 0 & 0 & 0 & \bar{\xi}^{-1} & \bar{\xi}^{-2} & 0 & 0 \\ 0 & 0 & 0 & 1 & 0 & 0 & \bar{t}_1^{-1} \bar{t}_1^{-2} \bar{\xi}^{-2} & \bar{t}_2^{-1} \bar{t}_2^{-2} \bar{\xi}^{-1} & 0 & 0 & 0 & 0 \\ 0 & 0 & 0 & 0 & 1 & 0 & 0 & 0 & 0 & 0 & \bar{t}_1^{-1} \bar{\xi}^{-2} & \bar{t}_2^{-1} \bar{\xi}^{-1} \\ 0 & 0 & 0 & 0 & 0 & 1 & 0 & 0 & 0 & 0 & \bar{t}_1^{-2} \bar{\xi}^{-2} & \bar{t}_2^{-2} \bar{\xi}^{-1} \end{bmatrix}, \quad (46)$$

where \bar{t}_α^β are the elements of the Jacobian matrix evaluated at the element center; $\bar{\xi}^\alpha$ are the transformed coordinates defined as

$$\bar{t}_1^\alpha = \frac{1}{4} (x_1^\alpha - x_2^\alpha - x_3^\alpha + x_4^\alpha), \quad \bar{t}_2^\alpha = \frac{1}{4} (x_1^\alpha + x_2^\alpha - x_3^\alpha - x_4^\alpha),$$

$$\bar{\xi}^\alpha = \xi^\alpha - \xi_c^\alpha, \quad \xi_c^\alpha = \frac{1}{A_{el}} \int_{-1}^1 \int_{-1}^1 \xi^\alpha \det(\mathbf{J}) d\xi^1 d\xi^2, \quad (47)$$

$$A_{el} = \int_{-1}^1 \int_{-1}^1 \det(\mathbf{J}) d\xi^1 d\xi^2.$$

The aim of introducing $\bar{\xi}^\alpha$ lies in simplicity of some element matrices of the hybrid-mixed method [44,45] because a useful formula

$$\int_{-1}^1 \int_{-1}^1 \bar{\xi}^\alpha \det(\mathbf{J}) d\xi^1 d\xi^2 = 0, \quad (48)$$

holds.

Remark 5. According to stress interpolations (44)–(46), 12 assumed stress parameters $\Phi_1^I, \Phi_2^I, \dots, \Phi_{12}^I$ are introduced for each SaS, i.e., $12N$ for all SaS. It seems to be excessive for the four-node quadrilateral plate element with $12N$ displacement DOF. However, there exist six dependent modes, which provide a correct rank of the element stiffness matrix [39].

Substituting interpolations (14), (15), (20) and (44) in a mixed variational equation (42) and considering Eq. (22), the nonlinear equilibrium equations of the hybrid-mixed plate element are obtained

$$\sum_J A^{IJ} [(\mathbf{R}^J(\mathbf{q}) - \mathbf{G}^J(\mathbf{q})) \mathbf{q} - \mathbf{Q}\Phi^J] = 0, \quad (49)$$

$$\sum_I \sum_J A^{IJ} (\mathbf{R}^I(\mathbf{q}))^T \Phi^J = \mathbf{F}, \quad (50)$$

where

$$\mathbf{Q} = \int_{-1}^1 \int_{-1}^1 \mathbf{P}^T \mathbf{C}^{-1} \mathbf{P} \det(\mathbf{J}) d\xi^1 d\xi^2,$$

$$\mathbf{R}^I(\mathbf{q}) = \int_{-1}^1 \int_{-1}^1 \mathbf{P}^T \mathbf{L}^I(\mathbf{q}) \det(\mathbf{J}) d\xi^1 d\xi^2, \quad (51)$$

$$\mathbf{G}^I(\mathbf{q}) = \int_{-1}^1 \int_{-1}^1 \mathbf{P}^T \mathbf{A}^I(\mathbf{q}) \det(\mathbf{J}) d\xi^1 d\xi^2.$$

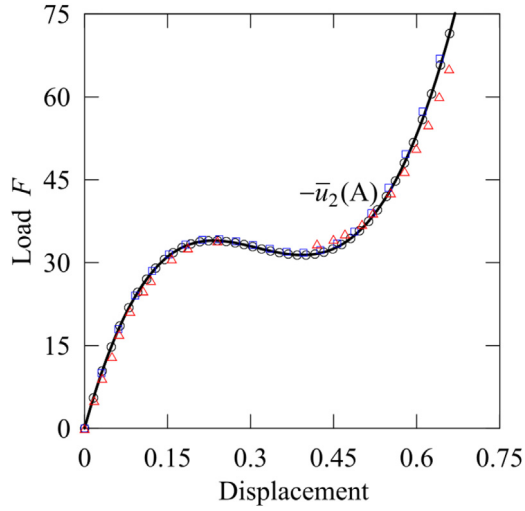


Fig. 7. Vertical displacement of the middle surface at point A of William's toggle frame versus load F : SaSH4 element using three SaS and 16×1 mesh for $\nu = 0$ (○) and $\nu = 0.3$ (□) and experimental study [46] (△).

Due to the fact that $\det(\Lambda^{IJ}) \neq 0$ [36], Eq. (49) can be simplified

$$(\mathbf{R}^I(\mathbf{q}) - \mathbf{G}^I(\mathbf{q})) \mathbf{q} = \mathbf{Q}\Delta\Phi^I. \quad (52)$$

Next, we implement the incremental total Lagrangian formulation

$${}^{t+\Delta t}\mathbf{q} = {}^t\mathbf{q} + \Delta\mathbf{q}, \quad {}^{t+\Delta t}\Phi^I = {}^t\Phi^I + \Delta\Phi^I, \quad {}^{t+\Delta t}\mathbf{F} = {}^t\mathbf{F} + \Delta\mathbf{F}, \quad (53)$$

where $\Delta\mathbf{q}$, $\Delta\Phi^I$ and $\Delta\mathbf{F}$ are the incremental variables. Substituting Eq. (53) in equilibrium equations (50) and (52) and considering that the external loads and stresses constitute the self-equilibrated system in a configuration at time t , the incremental equations are written as

$$(\mathbf{R}^I({}^t\mathbf{q} + \Delta\mathbf{q}) - \mathbf{G}^I(\Delta\mathbf{q})) \Delta\mathbf{q} = \mathbf{Q}\Delta\Phi^I, \quad (54)$$

$$\sum_I \sum_J \Lambda^{IJ} \left[(\mathbf{R}^I({}^t\mathbf{q} + \Delta\mathbf{q}))^T \Delta\Phi^J + 2(\mathbf{G}^I(\Delta\mathbf{q}))^T {}^t\Phi^J \right] = \Delta\mathbf{F}, \quad (55)$$

where the load vector $\Delta\mathbf{F}$ is defined by the scalar parameter $\Delta\varphi$ and the constant load vector $\bar{\mathbf{F}}$ as follows:

$$\sum_I \sum_J \Lambda^{IJ} \left[(\mathbf{R}^I({}^t\mathbf{q} + \Delta\mathbf{q}))^T \Delta\Phi^J + 2(\mathbf{G}^I(\Delta\mathbf{q}))^T {}^t\Phi^J \right] = \Delta\varphi \bar{\mathbf{F}}. \quad (56)$$

The Newton–Raphson iteration process is applied to linearize the non-linear terms in incremental equations (54) and (56) as

$$\begin{aligned} \Delta\mathbf{q}^{[n+1]} &= \Delta\mathbf{q}^{[n]} + \Delta\tilde{\mathbf{q}}^{[n]}, \\ \Delta\varphi^{[n+1]} &= \Delta\varphi^{[n]} + \Delta\tilde{\varphi}^{[n]}, \\ \Delta\Phi^{I[n+1]} &= \Delta\Phi^{I[n]} + \Delta\tilde{\Phi}^{I[n]}, \end{aligned} \quad (57)$$

$n = 0, 1, \dots, \text{NIter}$.

By substituting Eq. (57) in incremental equations, the following linearized equilibrium equations are obtained:

$$\begin{aligned} \mathbf{R}^I({}^t\mathbf{q} + \Delta\mathbf{q}^{[n]}) \Delta\tilde{\mathbf{q}}^{[n]} - \mathbf{Q}\Delta\tilde{\Phi}^{I[n]} & \\ = \mathbf{Q}\Delta\Phi^{I[n]} - (\mathbf{R}^I({}^t\mathbf{q} + \Delta\mathbf{q}^{[n]}) - \mathbf{G}^I(\Delta\mathbf{q}^{[n]})) \Delta\mathbf{q}^{[n]}, & \quad (58) \\ \sum_I \sum_J \Lambda^{IJ} \left[(\mathbf{R}^I({}^t\mathbf{q} + \Delta\mathbf{q}^{[n]})^T \Delta\tilde{\Phi}^{J[n]} + 2(\mathbf{G}^I(\Delta\tilde{\mathbf{q}}^{[n]}))^T ({}^t\Phi^J + \Delta\Phi^{J[n]}) \right] & \\ = (\Delta\varphi^{[n]} + \Delta\tilde{\varphi}^{[n]}) \bar{\mathbf{F}} & \end{aligned}$$

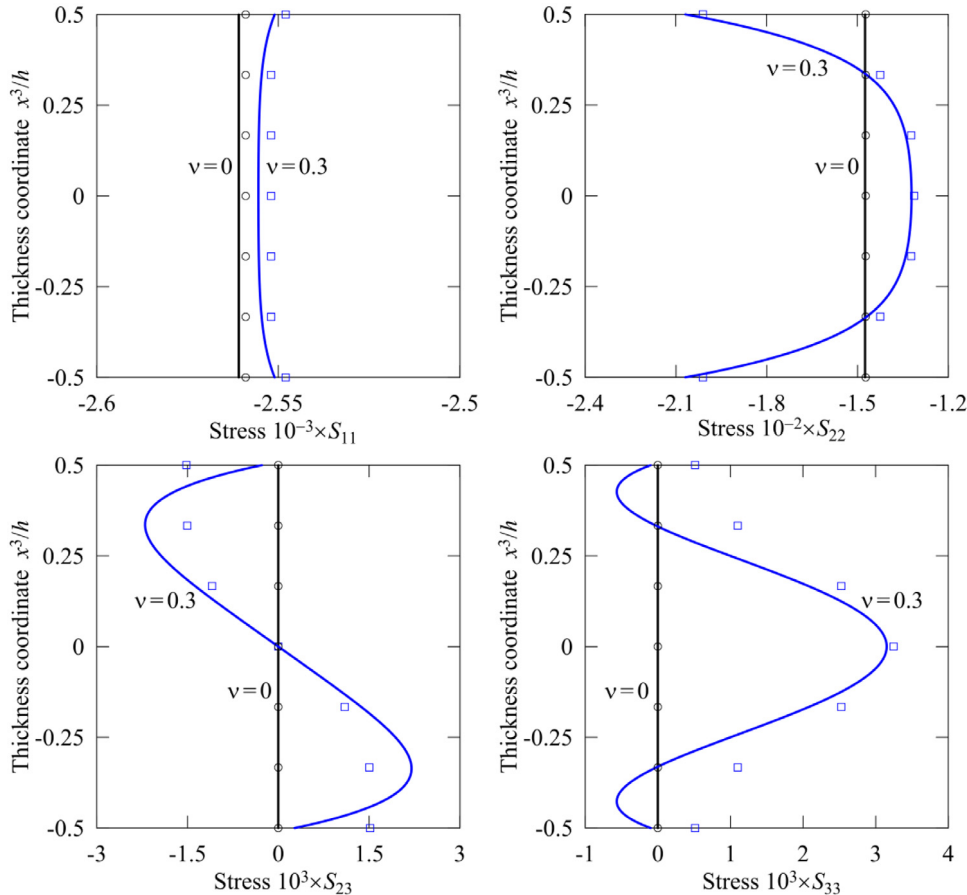


Fig. 8. Through-thickness distributions of the second Piola–Kirchhoff stresses for the William's toggle frame at point B under load $F = 30$: SaSH4 element using seven SaS and 128×8 mesh (solid lines), and SOLID45 element using $128 \times 8 \times 6$ mesh for $\nu = 0$ (○) and $\nu = 0.3$ (□).

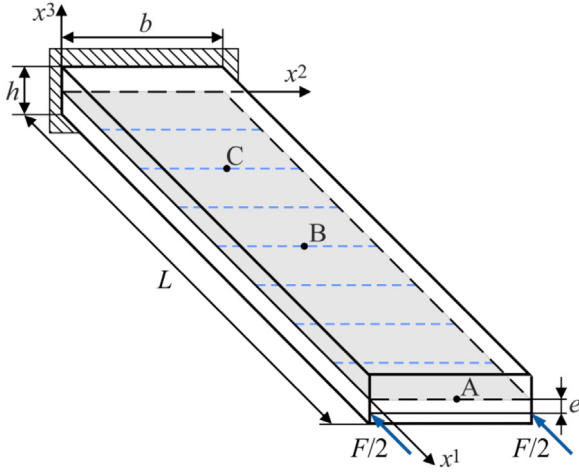


Fig. 9. Column with rectangular cross section under eccentric load with $-h/2 \leq e < 0$.

$$-\sum_I \sum_J \Lambda^{IJ} \left[(\mathbf{R}^I(\mathbf{t}\mathbf{q} + \Delta\mathbf{q}^{[n]}))^T \Delta\Phi^{J[n]} + 2(\mathbf{G}^I(\Delta\mathbf{q}^{[n]}))^T \mathbf{t}\Phi^J \right]. \quad (59)$$

Eliminating incremental stress parameters $\Delta\tilde{\Phi}^{I[n]}$ from Eqs. (58) and (59), the system of linear algebraic equations can be written as

$$\mathbf{K}_T \Delta\tilde{\mathbf{q}}^{[n]} = \Delta\mathbf{F}^{[n]} + \Delta\tilde{\varphi}^{[n]}\bar{\mathbf{F}}, \quad (60)$$

where $\mathbf{K}_T = \mathbf{K}_D + \mathbf{K}_H$ is the tangent stiffness matrix of order $12N \times 12N$; $\Delta\mathbf{F}^{[n]}$ is the right-hand side vector given by

$$\mathbf{K}_D = \sum_I \sum_J \Lambda^{IJ} (\mathbf{R}^I(\mathbf{t}\mathbf{q} + \Delta\mathbf{q}^{[n]}))^T \mathbf{Q}^{-1} \mathbf{R}^J(\mathbf{t}\mathbf{q} + \Delta\mathbf{q}^{[n]}), \quad (61)$$

$$\mathbf{K}_H = 2 \sum_I \sum_J \Lambda^{IJ} \mathbf{T}^I(\mathbf{t}\Phi^J + \Delta\Phi^{J[n]}), \quad (62)$$

$$\Delta\mathbf{F}^{[n]} = \Delta\varphi^{[n]}\bar{\mathbf{F}} - \sum_I \sum_J \Lambda^{IJ} \left[(\mathbf{R}^I(\mathbf{t}\mathbf{q} + \Delta\mathbf{q}^{[n]}))^T \mathbf{Q}^{-1} \times (\mathbf{R}^J(\mathbf{t}\mathbf{q} + \Delta\mathbf{q}^{[n]}) - \mathbf{G}^J(\Delta\mathbf{q}^{[n]})) + 2\mathbf{T}^I(\mathbf{t}\Phi^J) \right] \Delta\mathbf{q}^{[n]}, \quad (63)$$

where $\mathbf{T}^I(\Phi^J)$ are the symmetric matrices of order $12N \times 12N$ defined as

$$\mathbf{T}^I(\Phi^J) = \int_{-1}^1 \int_{-1}^1 \mathbf{H}^I(\mathbf{P}\Phi^J) \det(\mathbf{J}) d\xi^1 d\xi^2, \quad (64)$$

where the symmetric matrices $\mathbf{H}^I(\mathbf{w})$ are introduced in Appendix B.

Applying the cylindrical arc-length method, a quadratic equation similar to Eq. (38) for finding $\Delta\tilde{\varphi}^{[n]}$ can be derived. By selecting the proper solution $\Delta\tilde{\varphi}^{[n]}$, the incremental displacement vector $\Delta\tilde{\mathbf{q}}^{[n]}$ can be calculated using Eq. (60).

Remark 6. The hybrid-mixed ANS plate element formulation requires a numerical inversion of the matrix \mathbf{Q} of order 12×12 . As we remember, in the displacement-based ANS plate element formulation the element matrices (32)–(34) are evaluated with no numerical matrix inversion.

To calculate the incremental stress vectors $\Delta\Phi^{I[n]}$ from Eq. (62), we apply an advanced finite element technique based on the use of linearized equilibrium equations (54) at the previous n th iteration:

$$\Delta\Phi^{I[n]} = \mathbf{Q}^{-1} (\mathbf{R}^I(\mathbf{t}\mathbf{q} + \Delta\mathbf{q}^{[n-1]})\Delta\mathbf{q}^{[n]} - \mathbf{G}^I(\Delta\mathbf{q}^{[n-1]})\Delta\mathbf{q}^{[n-1]}). \quad (65)$$

These equations hold for $n \geq 1$ and at the beginning of each iteration process one should set

$$\Delta\mathbf{q}^{[0]} = \mathbf{0}, \quad \Delta\Phi^{I[0]} = \mathbf{0}. \quad (66)$$

The proposed incremental approach allows the use of the arc-length parameter, which are much larger than possible with the displacement-based finite element formulation. This is because the additional load

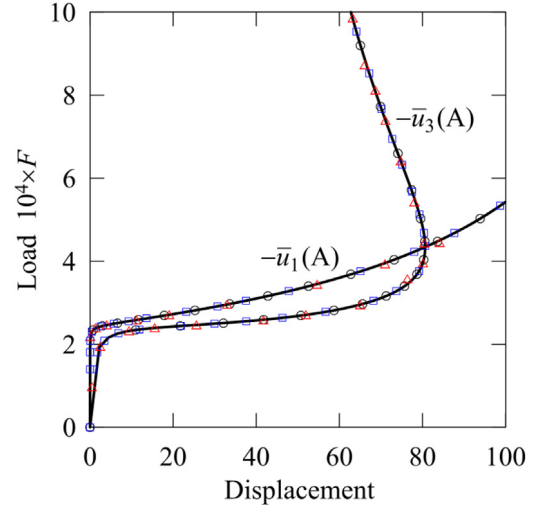


Fig. 10. Displacements of the middle surface at point A of the column versus load F with $e = -h/2$: SaSH4 element using three (○) and five (□) SaS and 32×1 mesh, and numerical results [47] (△).

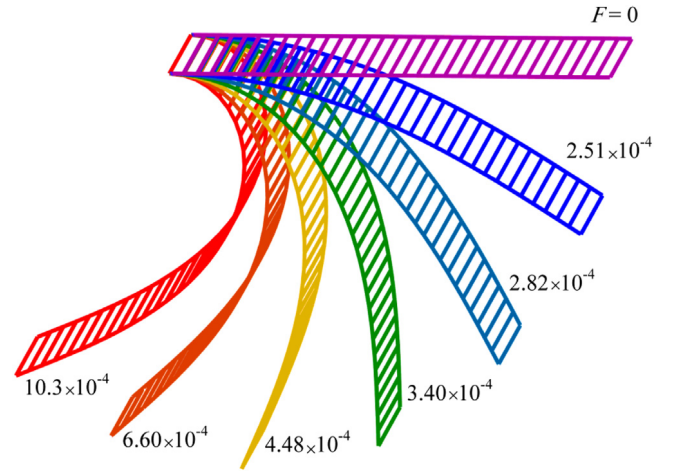


Fig. 11. Deformed configurations of the middle surface of the column under load F with $e = -h/2$ in different states: SaSH4 element using three SaS and 32×1 mesh.

vector due to compatibility mismatch (65) at the n th iteration step is presented in linearized equilibrium equations (60) and disappears only at the end of the iteration process as discussed in contributions [18,35,48].

4. Verification of SaS elements

The objectivity of the ANS plate quadrilaterals, denoted here by the SaSD4 (displacement based) and SaSH4 (hybrid-mixed) elements, is verified using the plate patch test and the inf-sup test and evaluating as well as their eigenvalues.

4.1. Patch test

The plate patch test for the bending behavior of quadrilateral elements confirms that the finite element formulation is able to reproduce the constant stress-strain states for distorted mesh configurations. Here, we consider a patch of five plate elements [49] with four external and four internal nodes depicted in Fig. 3.

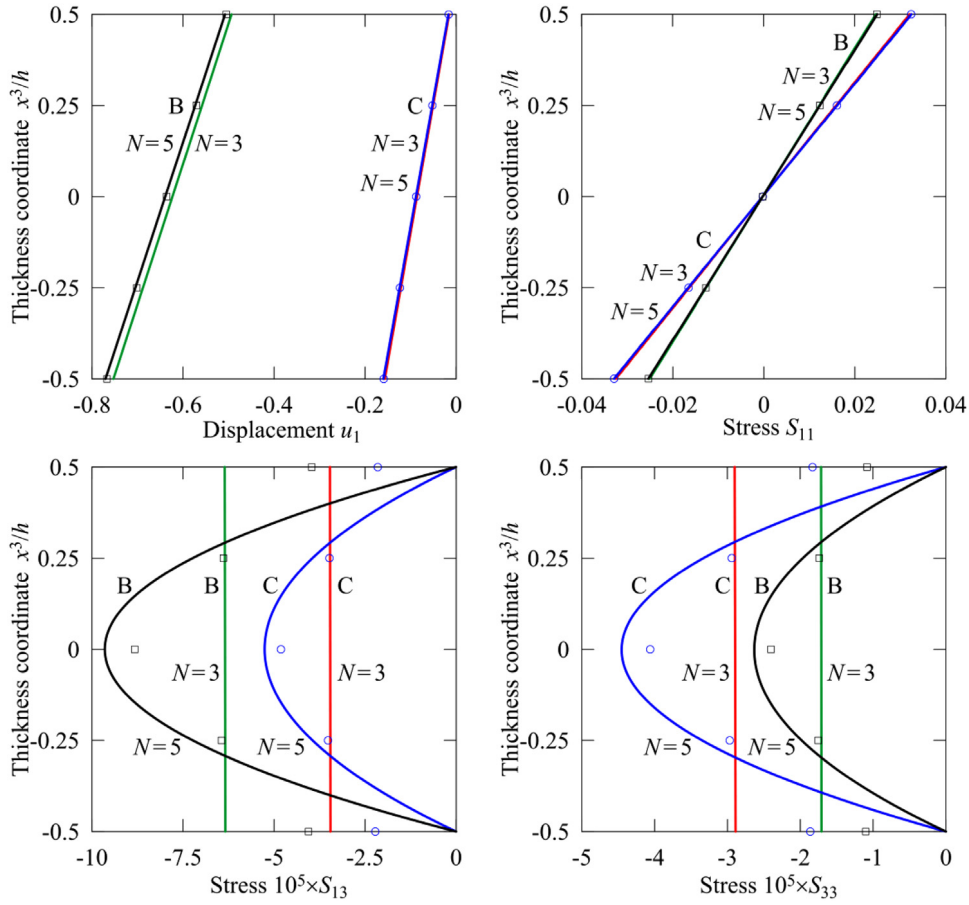


Fig. 12. Through-thickness distributions of the longitudinal displacement and second Piola–Kirchhoff stresses for the column under eccentric load $F = 2.45 \times 10^{-4}$ with $e = -h/2$ at points B and C: SaSH4 element using three and five SaS and 128×1 mesh (solid lines), and SOLID45 element using $128 \times 1 \times 4$ mesh (\square) and (\circ)

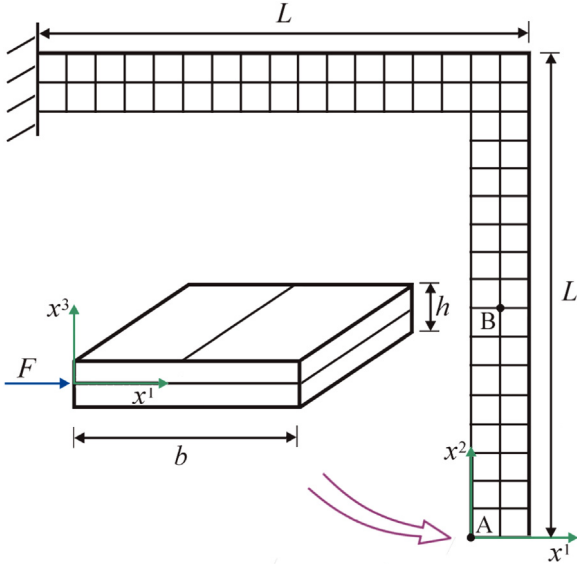


Fig. 13. L-shaped plate modeled by $16k^2$ square elements with dimensions b/k , where k is a number of elements along the width ($k = 2, 4, 6, 8$ and 16).

To fulfill the constant bending stress–strain state [39], the displacements of SaS are prescribed as

$$\begin{aligned} u_1^I &= ez^I \left(x^1 + \frac{1}{2}x^2 \right), & u_2^I &= ez^I \left(\frac{1}{2}x^1 + x^2 \right), \\ u_3^I &= -\frac{1}{2}e \left[(x^1)^2 + x^1x^2 + (x^2)^2 \right]. \end{aligned} \quad (67)$$

Applying prescribed displacements (67) to the external nodes, we find that the displacements and strains at the internal nodes are identical to analytical answers. This study was conducted in papers [39,50] by using three and five SaS and confirmed that the SaSD4 and SaSH4 elements pass the bending plate patch test.

4.2. Eigenvalue analysis

Here, we present the solution of the eigenvalue problem for one half of the toggle frame (see Fig. 4) using a single element with three and five SaS inside the frame. The geometric and material parameters of the toggle are given in Section 5.1. The calculations are performed using SaSD4 and SaSH4 elements and the results are shown in Fig. 5. It is seen that six zero eigenvalues are clearly observed for both finite element formulations. These numerical results confirm the results of a theoretical study [39].

4.3. Inf-sup test

Finally, we implement the inf-sup condition [51] for the developed SaS quadrilaterals. To perform the inf-sup test, we have to solve the generalized eigenvalue problem [52]

$$\tilde{\mathbf{K}}\mathbf{U} = \lambda\tilde{\mathbf{M}}\mathbf{U}, \quad (68)$$

where $\tilde{\mathbf{K}}$ is the global stiffness matrix; $\tilde{\mathbf{M}}$ is the norm matrix, which can be obtained using the standard assembly procedure for the element mass matrix with a unit material density

$$\mathbf{M} = \int_{-1}^1 \int_{-1}^1 \sum_I \sum_J A^{IJ} (\mathbf{N}^I)^T \mathbf{N}^J \det(\mathbf{J}) d\xi_1 d\xi_2 \quad (69)$$

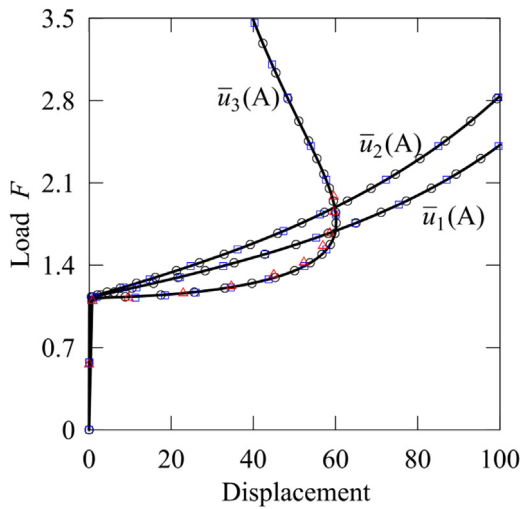


Fig. 14. Displacements of the middle surface at point A of the L-shaped plate versus load F : SaSH4 element using three (○) and five (□) SaS and mesh parameter $k = 4$, and numerical results [53] (△).

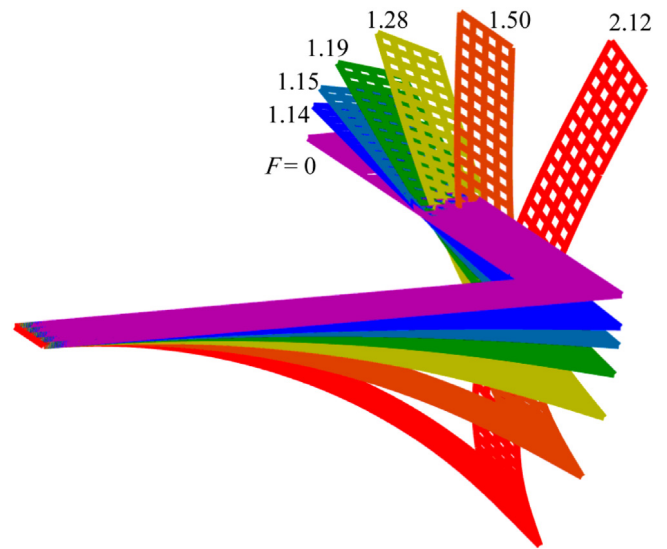


Fig. 15. Deformed configurations of the middle surface of the L-shaped plate in different states: SaSH4 element using three SaS and mesh parameter $k = 4$.

Table 4
Critical load of the L-shaped plate with $e = h/50$ using three SaS and $\Delta\ell = 1$.

Element	Mesh parameter k	F
SaSD4	2	1.139
	4	1.128
	6	1.124
	8	1.123
SaSH4	2	1.135
	4	1.126
	6	1.123
	8	1.122
Simo et al. [54]	–	1.128
Campello et al. [53]	–	1.130
Wriggers and Gruttmann [55]	–	1.123

Table 5
Critical load of the circular plate with $e = -h/10^4$ using three SaS and $\Delta\ell = 10^{-2}$.

Element	Mesh parameter k	$10^{-6} \times P$
SaSD4	2	10.417
	4	10.633
	8	10.686
	16	10.699
SaSH4	2	10.405
	4	10.631
	8	10.685
	16	10.699
Timoshenko and Gere [43]	–	10.769

Table 6
Results for the circular plate with $e = -h/100$ using three SaS, mesh parameter $k = 8$ and NStat = 1.

Element	$\Delta\ell$	50	100	150	200	250
SaSD4	NIter	6	8	11	25	14
	$10^{-6} \times P$	33.69	83.64	158.2	268.7	459.6
	$\bar{u}_3(A)$	2.947	5.325	7.460	9.477	11.390
SaSH4	NIter	6	7	7	8	9
	$10^{-6} \times P$	33.61	83.12	156.5	265.2	457.5
	$\bar{u}_3(A)$	2.947	5.321	7.447	9.453	11.348

similar to the assembly of the element stiffness matrix \mathbf{K} , where \mathbf{N}^I are the shape function matrices of order $3 \times 12N$ defined by finite element approximations of the SaS displacements $\mathbf{u}^I = \mathbf{N}^I \mathbf{q}$. The nonzero components of these matrices are found as

$$(\mathbf{N}^I)_{i,i+3(I-1)+3N(r-1)} = N_r, \tag{70}$$

where N_r are the bilinear shape functions (16); the indices $i = 1, 2, 3$, $I = 1, 2, \dots, N$ and $r = 1, 2, 3, 4$.

The numerical algorithm consists in calculating the smallest nonzero eigenvalue λ_{\min} of the generalized eigenvalue problem (68) for a specified mesh. As a numerical example, consider one half of the toggle frame (Fig. 4) clamped on the left edge ($u_1^l = u_2^l = 0$) and symmetrically supported on the right ($u_1^r = 0$). The geometric and material parameters of the toggle are given in Section 5.1. The results obtained by SaSD4 and SaSH4 elements for the different Poisson's ratios using three SaS and two families of distorted meshes $2k \times 1$ and $8k \times k$, where $k = 1, 2, 4, 8, 16$ and 32 , are shown in Fig. 6. As can be seen, both SaS elements pass the inf-sup test for all values of the Poisson's ratio but the SaSH4 element behaves much better. Note also that the use of a larger number of SaS inside the frame body leads to very close results for the smallest nonzero eigenvalue. For example, the SaSH4 element using a 8×1 mesh and Poisson's ratio of 0.499 provides the following results: $\log_{10}(\lambda_{\min}) = 2.2835$ and 2.2831 for three and five SaS, respectively.

5. Numerical results

The performance of SaSD4 and SaSH4 elements are evaluated using analytical and finite element solutions extracted from the literature and experimental results as well. Herein, to plot the load–displacement curves, Eqs. (36) and (60) are applied to some states with the incremental arc-length parameter $\Delta\ell$. Note also that NStat denotes a number of states and NIter stands for a total number of iterations required to reach the prescribed tolerance of $\epsilon = 10^{-4}$.

5.1. William's toggle frame

In this section, a two bar frame frequently used in the literature for the nonlinear structural analysis is selected to verify the accuracy of the implementation of the arc-length method for both finite elements. The frame with clamped edges is subjected to vertical load at the top as shown in Fig. 4. The geometric and material parameters of the frame are chosen as $L_1 = 12.943$, $L_2 = 0.386$, $b = 0.243$, $h = 0.753$, $E =$

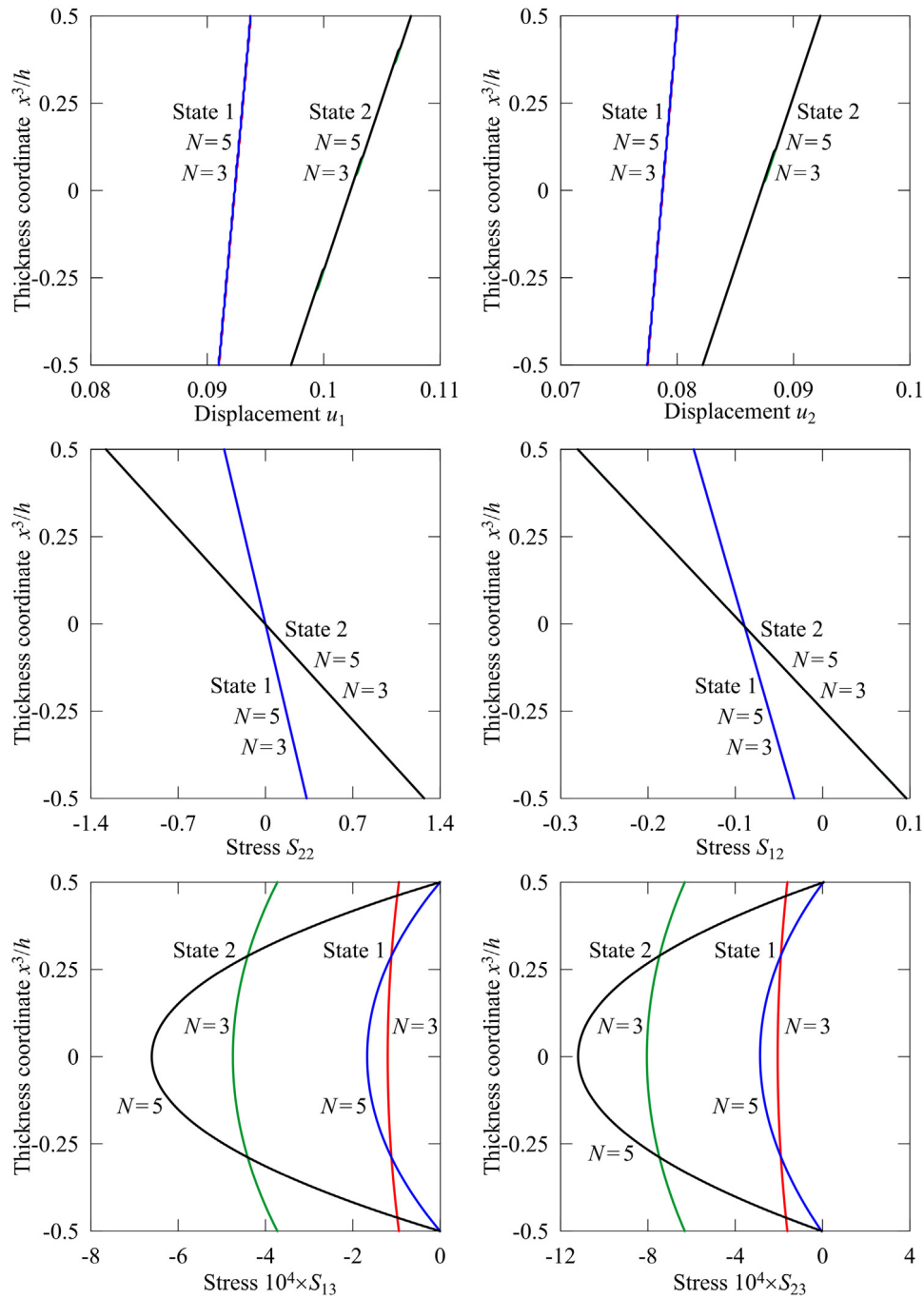


Fig. 16. Through-thickness distributions of in-plane displacements and second Piola–Kirchhoff stresses for the L-shaped plate at point B(15, 120) in two states near bifurcation: SaSH4 element using three and five SaS and mesh parameter $k = 16$.

10.3×10^6 , $\nu = 0$ and $\nu = 0.3$ as well. The analytical and experimental results for the frame are presented by Williams [46], whereas the numerical results are given by many authors (see e.g. [47]). According to numerical and experimental studies, a moderate snap-through is reported in the variation of load F versus the vertical displacement of the middle surface \bar{u}_2 (A). Due to symmetry of the problem, only one half of the frame is modeled by $4k \times 1$ meshes.

The results of the convergence study for $\nu = 0$ are given in Table 1. It is seen that the SaSH4 element converges very fast and allows the use of coarse meshes to achieve reasonable results. On the contrary, the SaSD4 element with the same incremental arc-length parameter $\Delta \ell$ requires the use of only fine meshes. Fig. 7 displays the load–displacement curves using the SaSH4 element with three SaS and 16×1

mesh for two values of Poisson’s ratios compared with the results of the experimental study [46]. The results corresponding to five SaS are not plotted because they are graphically indistinguishable. Fig. 8 shows the through-thickness distribution of the second Piola–Kirchhoff stress tensor at point B under load $F = 30$ using seven SaS and a fine 128×8 mesh to describe well boundary conditions on the external surfaces for the transverse stresses because these stresses are small. The results are compared with those obtained by the ANSYS SOLID45 element [56] using $128 \times 8 \times 6$ mesh that corresponds to a selected number of SaS. These results demonstrate the high potential of the SaSH4 element, since the boundary conditions for the transverse stresses are satisfied correctly and cannot be reproduced using a less number of SaS due to the non-parabolic distribution of the transverse stresses. Note also

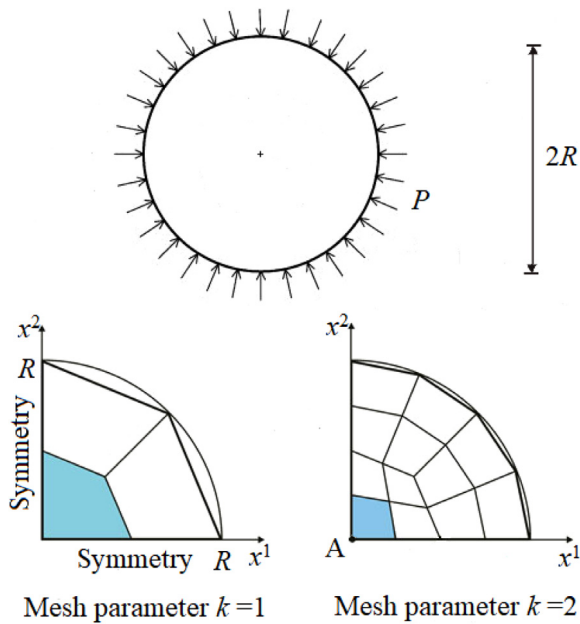


Fig. 17. One quarter of the circular plate modeled by distorted meshes of $3k^2$ elements, where $k = 1, 2, 4, 8, 16$ and 24 .

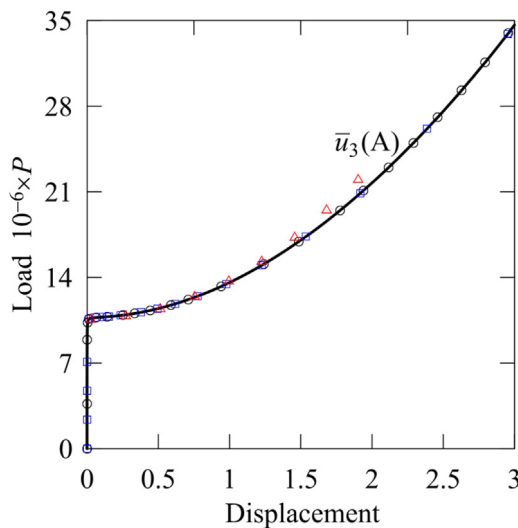


Fig. 18. Transverse displacement of the middle surface at point A of the circular plate versus load P : SaSH4 element using three (\square) and five (\circ) SaS and mesh parameter $k = 8$, and semi-analytical solution [57] (\triangle).

that the SOLID45 element leads to poor prediction of these stresses for $\nu = 0.3$. As it turned out, it is impossible to fulfill the boundary conditions for transverse stresses choosing more elements across the thickness.

5.2. Column under eccentric load

In this example, a column with a rectangular cross section is considered. One edge is clamped and the other is free and subjected to two concentrated eccentric loads as shown in Fig. 9. The geometric parameters and material properties are taken as $L = 100, b = h = 1, E = 12$ and $\nu = 0$. Due to eccentric loading ($-h/2 \leq e < 0$), there is no bifurcation-type buckling. However, the critical load can be estimated in very small values of $|e|$. Therefore, the convergence study of the critical load using both SaS elements is presented in Table 2 applying

$e = -h/10^4$ and calculating the intersection of the primary equilibrium path and quadratic fitting of the load–displacement curve. It is seen that the SaS elements require relatively coarse meshes to match the result of Timoshenko and Gere [43]. A comparison of the number of iterations in predicting the second state from the initial state (NStat = 1) obtained by the SaSD4 and SaSH4 elements is shown in Table 3. Here, it is assumed that the compression load is positioned on the bottom surface, that is, $e = -h/2$. As can be seen, in low values of the arc-length parameter, both elements are similar. However, in prediction of very far states using large values of $\Delta \ell$, the SaSH4 element is more efficient. The load–displacement curves related to point A are shown in Fig. 10. A good agreement is seen between the current results using three and five SaS and 32×1 mesh and those obtained by Wood and Zienkiewicz [47]. The deformed configurations of the middle surface are plotted in Fig. 11. Fig. 12 presents through-thickness distributions of the longitudinal displacement and second Piola–Kirchhoff stresses at points B and C using three and five SaS and a fine mesh 128×1 . Here, a state near the critical load with $F = 2.45 \times 10^{-4}$ is considered. A comparison is made with the SOLID45 element [56] using $128 \times 1 \times 4$ mesh. The non-displayed stress components are zeros. The results using five SaS demonstrate again the high potential of the SaSH4 element because the boundary conditions on the bottom and top surfaces for transverse stresses are satisfied with very high accuracy. However, the use of three SaS that corresponds to applying a 9-parameter higher-order theory (see e.g. [26,27,29]) yields unacceptable results for the transverse shear and normal stresses.

5.3. L-shaped plate

Consider a cantilever L-shaped plate subjected to in-plane force F on the middle surface at point A as depicted in Fig. 13. The geometric parameters and material properties are $L = 255, b = 30, h = 0.6, E = 71240$ and $\nu = 0.31$. The plate is modeled by square elements characterized by a mesh parameter k , which defines the number of elements along the plate width, where $k = 2, 4, 6, 8$ and 16 . In such situation, the total number of elements is $16k^2$. This problem has been considered by many researchers [53–55,58–60]. They apply a small perturbation in out of plane to obtain the secondary equilibrium path. Here, the SaS formulation is used to trigger the secondary equilibrium path by applying the in-plane force with a small eccentricity. This condition is beneficial for different shapes of structures, since a position of the perturbation load may have an effect on the buckling modes.

Table 4 shows the results of the convergence study for both SaS elements, which are obtained by finding the intersection point of primary equilibrium path and quadratic fitting of the load–deflection curve. The results are compared with those found in papers [53–55]. It is seen that the results agree well even in the case of coarse meshes. Fig. 14 displays the displacements of the middle surface at point A versus load F using the SaSH4 element with three and five SaS and mesh parameter $k = 4$. The transverse displacement $\bar{u}_3(A)$ is compared with the numerical solution of Campello et al. [53] and one can see that a good agreement is achieved until $\bar{u}_3(A) \leq 60$. It is also seen that the transverse displacement is decreased and the current path-following method, that is, the arc-length method, calculates the correct states. The deformed configurations of the L-shaped plate are depicted in Fig. 15. As can be seen, the transverse displacement at point A is increased and then decreased. Fig. 16 shows the through-thickness distribution of the displacements and second Piola–Kirchhoff stress tensor at point B (15, 120) in State 1 ($F = 1.087$ and $\bar{u}_3(A) = 0.564$) and State 2 ($F = 1.113$ and $\bar{u}_3(A) = 2.222$) using three and five SaS and mesh parameter $k = 16$. Obviously, the displacement increments cause a strong change in the stress distribution. As can be seen, the SaSH4 element performs well, since the boundary conditions on outer surfaces for transverse shear components are fulfilled properly. However, it cannot be employed for the calculation of the transverse normal stress because the plate is very thin with the slenderness ratio of $L/h = 425$. For thicker plates, there is no such problem as established in works [35,36] using exact geometry SaS solid-shell elements.

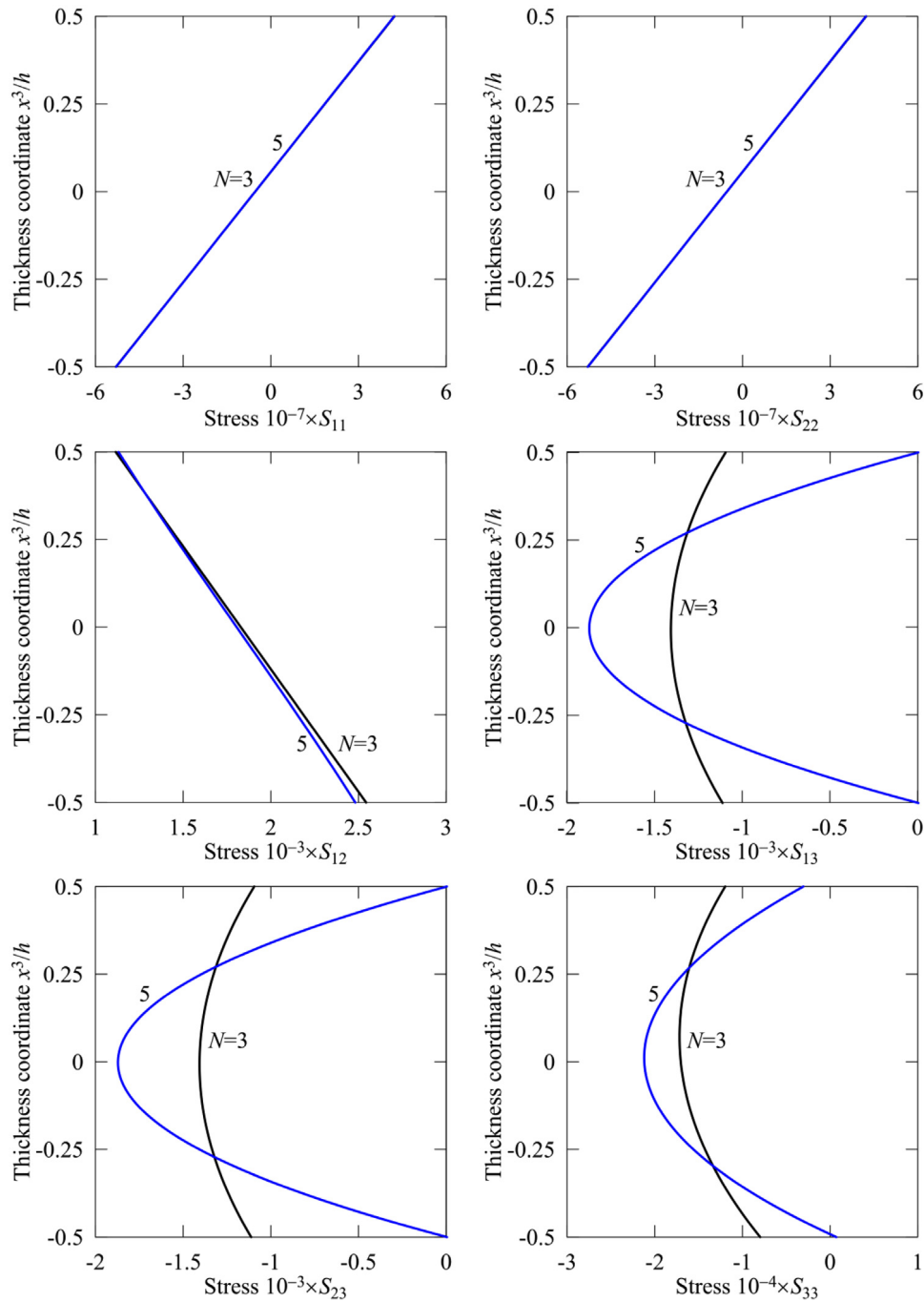


Fig. 19. Through-thickness distribution of the second Piola-Kirchhoff stress tensor for the circular plate at point A in a post-buckling state: SaSH4 element using three and five SaS and mesh parameter $k = 24$.

5.4. Circular plate under uniform in-plane pressure

To evaluate the effect of mesh distortion on performance of SaS elements, we consider a circular plate with simply supported boundary conditions subjected to uniform in-plane pressure P (force per unit length) as depicted in Fig. 17. Due to symmetry, only one quarter of the plate is modeled by distorted meshes of $3k^2$ elements, where $k = 1, 2, 4, 8, 16$ and 24 . The geometric parameters and mechanical properties are taken as $R = 50$, $h = 1$, $E = 70 \times 10^9$ and $\nu = 0.3$. The in-plane pressure is applied with a very small eccentricity to trigger the secondary equilibrium path.

Table 5 presents the results of the convergence study for the SaS quadrilateral elements. The critical load is defined as the intersection

point of primary equilibrium path and quadratic fitting of the load-displacement curve. It is seen that both SaS elements allow the use of coarse meshes and the results agree closely with the exact solution of Timoshenko and Gere [43]. The results listed in Table 6 have been found for $NStat = 1$ and demonstrate again that the SaSH4 element is the best performer especially for far states. Fig. 18 shows the load-displacement curve using the SaSH4 element with three and five SaS and mesh parameter $k = 8$ compared with the semi-analytical solution [57]. In this work, a first-order shear deformation theory and von Karman strain-displacement equations are applied. Therefore, the results are close only in a region $\bar{u}_3(A) \leq 1$. Fig. 19 displays the through-thickness distribution of the second Piola-Kirchhoff stress tensor at point A in a state of post-buckling regime ($P = 13.3 \times 10^6$ and $\bar{u}_3(A) =$

0.99) using the SaSH4 element with three and five SaS inside the plate and a fine mesh with the mesh parameter $k = 24$. As can be seen, the use of the 15-parameter model with five SaS inside the plate leads to good accuracy in fulfilling the boundary conditions on the bottom and top surfaces for transverse shear stresses. However, this model describes worse boundary conditions for the transverse normal stress. This is due to the fact that this stress is very small and the use of distorted meshes does not allow us to find a better solution of the problem. Note also that again the 9-parameter model with three SaS yields unacceptable results for the transverse stress components.

6. Conclusions

This paper presents the ANS displacement-based (SaSD4) and hybrid-mixed (SaSH4) quadrilateral elements based on the SaS formulation for the 3D stress analysis of plate-type structures in instability conditions. Two key points are considered in the SaS formulation: the displacements, strains and stresses are interpolated in the thickness direction using Lagrange polynomials, and the locations of SaS are associated with Chebyshev polynomial nodes. The nonlinear equilibrium equations are solved by the Newton–Raphson method combined with the Crisfield arc-length algorithm. The obtained results indicate convincingly the high potential of both SaS elements in predicting different critical points. However, the SaSH4 element converges faster and the number of Newton iterations can be significantly reduced compared to the SaSD4 element. In addition, the SaSH4 element can be applied for the 3D stress analysis of different states such as pre-buckling, bifurcation and post-buckling with high accuracy in fulfilling boundary conditions.

Declaration of competing interest

The authors declare that they have no known competing financial interests or personal relationships that could have appeared to influence the work reported in this paper.

Acknowledgments

The work of G.M. Kulikov and S.V. Plotnikova was supported by the Russian Science Foundation under Grant No. 18-19-00092. The authors thank A.O. Glebov for help with the finite element evaluation in Sections 5.1 and 5.2.

Appendix A

Using interpolation (15), we can represent the SaS strain parameters (6) as

$$\begin{aligned} \lambda_{i\alpha}^I &= \sum_r \frac{\partial N_r}{\partial x^\alpha} u_{ir}^I, \\ \beta_i^I &= \sum_J M^J(x_3^I) \sum_r N_r u_{ir}^J. \end{aligned} \tag{A.1}$$

The derivatives of shape functions are taken as

$$\begin{bmatrix} \frac{\partial N_r}{\partial x^\alpha} \\ \frac{\partial N_r}{\partial x^\beta} \end{bmatrix} = \mathbf{J}^{-1} \begin{bmatrix} \frac{\partial N_r}{\partial \xi^1} \\ \frac{\partial N_r}{\partial \xi^2} \end{bmatrix}, \tag{A.2}$$

where $\mathbf{J} = \begin{bmatrix} J_\alpha^\beta \end{bmatrix}$ is the Jacobian matrix and $\mathbf{J}^{-1} = \begin{bmatrix} \ell_\alpha^\beta \end{bmatrix}$ is the inverse Jacobian matrix; their elements are defined as

$$\begin{aligned} t_1^\alpha &= \frac{1}{4} (1 + \xi^2) (x_1^\alpha - x_2^\alpha) + \frac{1}{4} (1 - \xi^2) (x_4^\alpha - x_3^\alpha), \\ t_2^\alpha &= \frac{1}{4} (1 + \xi^1) (x_1^\alpha - x_4^\alpha) + \frac{1}{4} (1 - \xi^1) (x_2^\alpha - x_3^\alpha), \\ \ell_1^1 &= \frac{1}{\Delta} t_2^2 \quad \ell_1^2 = -\frac{1}{\Delta} t_1^2 \quad \ell_2^1 = -\frac{1}{\Delta} t_2^1 \quad \ell_2^2 = \frac{1}{\Delta} t_1^1, \end{aligned} \tag{A.3}$$

where $\Delta = t_1^1 t_2^2 - t_1^2 t_2^1$.

The application of Eqs. (5) and (16)–(18), (A1) and (A2) leads to the presentation of SaS strains inside the quadrilateral plate element

$$\epsilon^I = \begin{bmatrix} \mathbf{B}_1^I \\ \mathbf{B}_2^I \\ \mathbf{B}_3^I \\ \mathbf{B}_4^I \\ \mathbf{B}_5^I \\ \mathbf{B}_6^I \end{bmatrix} \mathbf{q} + \begin{bmatrix} \Psi_1^I(\mathbf{q}) \\ \Psi_2^I(\mathbf{q}) \\ \Psi_3^I(\mathbf{q}) \\ \Psi_4^I(\mathbf{q}) \\ \Psi_5^I(\mathbf{q}) \\ \Psi_6^I(\mathbf{q}) \end{bmatrix}, \tag{A.4}$$

where $\mathbf{B}_s^I \mathbf{q}$ and $\Psi_s^I(\mathbf{q})$ are the linear and nonlinear parts of strain–displacement equations, where $s = 1, 2, \dots, 6$. The matrices \mathbf{B}_s^I are given in paper [50].

The matrices Π_s^I used in Eq. (21) are

$$(\Pi_s^I)_{\kappa\lambda} = \frac{1}{2} \frac{\partial^2 \Psi_s^I(\mathbf{q})}{\partial q_\kappa \partial q_\lambda}, \quad \kappa, \lambda = 1, 2, \dots, 12N. \tag{A.5}$$

It is apparent that matrices Π_s^I are symmetric.

Appendix B

Proposition 1. For any vector $\mathbf{w} = [w_1 w_2 w_3 w_4 w_5 w_6]^T$ the identity

$$(\mathbf{A}^I(\mathbf{q}))^T \mathbf{w} = \mathbf{H}^I(\mathbf{w}) \mathbf{q} \tag{B.1}$$

holds, where $\mathbf{H}^I(\mathbf{w})$ are the symmetric matrices of order $12N \times 12N$ given by

$$\mathbf{H}^I(\mathbf{w}) = \sum_s w_s \Pi_s^I. \tag{B.2}$$

Proof. The symmetry of matrices $\mathbf{H}^I(\mathbf{w})$ follows from the symmetry of matrices Π_s^I (see Appendix A). Due to Eq. (21), we have

$$(\mathbf{A}^I(\mathbf{q}))^T \mathbf{w} = [\Pi_1^I \mathbf{q} \quad \Pi_2^I \mathbf{q} \quad \Pi_3^I \mathbf{q} \quad \Pi_4^I \mathbf{q} \quad \Pi_5^I \mathbf{q} \quad \Pi_6^I \mathbf{q}] \mathbf{w} = \mathbf{H}^I(\mathbf{w}) \mathbf{q} \tag{B.3}$$

that completes the proof.

References

- [1] R. De Borst, M.A. Crisfield, J.J. Remmers, C.V. Verhoosel, *Nonlinear Finite Element Analysis of Solids and Structures*, John Wiley & Sons, 2012.
- [2] J.L. Batoz, G. Dhatt, Incremental displacement algorithms for nonlinear problems, *Internat. J. Numer. Methods Engrg.* 14 (8) (1979) 1262–1267.
- [3] S.L. Chan, Geometric and material non-linear analysis of beam–columns and frames using the minimum residual displacement method, *Internat. J. Numer. Methods Engrg.* 26 (12) (1988) 2657–2669.
- [4] Y.B. Yang, M.S. Shieh, Solution method for nonlinear problems with multiple critical points, *AIAA J.* 28 (12) (1990) 2110–2116.
- [5] K.J. Bathe, E.N. Dvorkin, On the automatic solution of nonlinear finite element equations, *Comput. Struct.* 17 (5–6) (1983) 871–879.
- [6] Y.B. Yang, W. McGuire, Stiffness matrix for geometric nonlinear analysis, *J. Struct. Eng.* 112 (4) (1986) 853–877.
- [7] G.A. Wempner, Discrete approximations related to nonlinear theories of solids, *Int. J. Solids Struct.* 7 (11) (1971) 1581–1599.
- [8] E. Riks, The application of Newton’s method to the problem of elastic stability, *J. Appl. Mech.* 39 (4) (1972) 1060–1065.
- [9] E. Riks, An incremental approach to the solution of snapping and buckling problems, *Int. J. Solids Struct.* 15 (7) (1979) 529–551.
- [10] H.B. Keller, Numerical solution of bifurcation and nonlinear eigenvalue problems, in: P. Rabinowitz (Ed.), *Applications of Bifurcation Theory*, Academic Press, New York, 1977, pp. 359–384.
- [11] E. Ramm, Strategies for tracing the nonlinear response near limit points, in: W. Wunderlich, E. Stein, K.J. Bathe (Eds.), *Nonlinear Finite Element Analysis in Structural Mechanics*, Springer, Berlin, Heidelberg, 1981, pp. 63–89.
- [12] M.A. Crisfield, A fast incremental/iterative solution procedure that handles snap-through, *Comput. Struct.* 13 (1–3) (1981) 55–62.
- [13] K.H. Schweizerhof, P. Wriggers, Consistent linearization for path following methods in nonlinear FE analysis, *Comput. Methods Appl. Mech. Engrg.* 59 (3) (1986) 261–279.
- [14] P.X. Bellini, A. Chulya, An improved automatic incremental algorithm for the efficient solution of nonlinear finite element equations, *Comput. Struct.* 26 (1–2) (1987) 99–110.
- [15] E. Carrera, A study on arc-length-type methods and their operation failures illustrated by a simple model, *Comput. Struct.* 50 (2) (1994) 217–229.

- [16] Y.H. Kim, S.W. Lee, A solid element formulation for large deflection analysis of composite shell structures, *Comput. Struct.* 30 (1–2) (1988) 269–274.
- [17] N. Büchter, E. Ramm, D. Roehl, Three-dimensional extension of non-linear shell formulation based on the enhanced assumed strain concept, *Internat. J. Numer. Methods Engrg.* 37 (15) (1994) 2551–2568.
- [18] H.C. Park, C. Cho, S.W. Lee, An efficient assumed strain element model with six DOF per node for geometrically non-linear shells, *Internat. J. Numer. Methods Engrg.* 38 (24) (1995) 4101–4122.
- [19] K.Y. Sze, W.K. Chan, T.H. Pian, An eight-node hybrid-stress solid-shell element for geometric non-linear analysis of elastic shells, *Internat. J. Numer. Methods Engrg.* 55 (7) (2002) 853–878.
- [20] H. Parisch, A continuum-based shell theory for non-linear applications, *Internat. J. Numer. Methods Engrg.* 38 (11) (1995) 1855–1883.
- [21] C. Sansour, A theory and finite element formulation of shells at finite deformations involving thickness change: circumventing the use of a rotation tensor, *Arch. Appl. Mech.* 65 (3) (1995) 194–216.
- [22] Y. Başar, M. Itskov, A. Eckstein, Composite laminates: nonlinear interlaminar stress analysis by multi-layer shell elements, *Comput. Methods Appl. Mech. Engrg.* 185 (2–4) (2000) 367–397.
- [23] R.A. Arciniega, J.N. Reddy, Tensor-based finite element formulation for geometrically nonlinear analysis of shell structures, *Comput. Methods Appl. Mech. Engrg.* 196 (4–6) (2007) 1048–1073.
- [24] G.M. Kulikov, S.V. Plotnikova, Finite rotation geometrically exact four-node solid-shell element with seven displacement degrees of freedom, *Comput. Model. Eng. Sci.* 28 (1) (2008) 15–38.
- [25] H.B. Soares, R.R. Paccola, H.B. Coda, Unconstrained vector positional shell FEM formulation applied to thin-walled members instability analysis, *Thin-Walled Struct.* 136 (2019) 246–257.
- [26] G.M. Kulikov, S.V. Plotnikova, Non-linear exact geometry 12-node solid-shell element with three translational degrees of freedom per node, *Internat. J. Numer. Methods Engrg.* 88 (13) (2011) 1363–1389.
- [27] B. Wu, A. Pagani, M. Filippi, W.Q. Chen, E. Carrera, Large-deflection and post-buckling analyses of isotropic rectangular plates by Carrera Unified Formulation, *Int. J. Non-Linear Mech.* 116 (2019) 18–31.
- [28] J.L. Mantari, F.G. Canales, Compact and unified elasto-plastic formulation to study isotropic plates, *J. Non-Linear Mech.* 118 (2020) 103253.
- [29] A. Pagani, E. Daneshkhah, X. Xu, E. Carrera, Evaluation of geometrically nonlinear terms in the large-deflection and post-buckling analysis of isotropic rectangular plates, *Int. J. Non-Linear Mech.* 121 (2020) 103461.
- [30] M. Amabili, A new nonlinear higher-order shear deformation theory with thickness variation for large-amplitude vibrations of laminated doubly curved shells, *J. Sound Vib.* 332 (19) (2013) 4620–4640.
- [31] M. Amabili, J.N. Reddy, The nonlinear third-order thickness and shear deformation theory for statics and dynamics of laminated composite shells, *Compos. Struct.* 244 (2020) 112265.
- [32] G.M. Kulikov, S.V. Plotnikova, On the use of sampling surfaces method for solution of 3D elasticity problems for thick shells, *ZAMM Z. Angew. Math. Mech.* 92 (11–12) (2012) 910–920.
- [33] G.M. Kulikov, S.V. Plotnikova, Solution of three-dimensional problems for thick elastic shells by the method of reference surfaces, *Mech. Solids* 49 (4) (2014) 403–412.
- [34] N.S. Bakhvalov, *Numerical Methods: Analysis, Algebra, Ordinary Differential Equations*, MIR Publishers, Moscow, 1977.
- [35] G.M. Kulikov, S.V. Plotnikova, Analysis of the second Piola–Kirchhoff stress in nonlinear thick and thin structures using exact geometry SaS solid-shell elements, *Internat. J. Numer. Methods Engrg.* 117 (5) (2019) 498–522.
- [36] G.M. Kulikov, S.V. Plotnikova, Finite rotation exact geometry solid-shell element for laminated composite structures through extended SaS formulation and 3D analytical integration, *Internat. J. Numer. Methods Engrg.* 119 (9) (2019) 852–878.
- [37] T.J.R. Hughes, T.E. Tezduyar, Finite elements based upon mindlin plate theory with particular reference to the four-node bilinear isoparametric element, *J. Appl. Mech.* 48 (1981) 587–596.
- [38] E.N. Dvorkin, K.J. Bathe, A continuum mechanics based four-node shell element for general non-linear analysis, *Eng. Comput.* 1 (1984) 77–88.
- [39] G.M. Kulikov, S.V. Plotnikova, A hybrid-mixed four-node quadrilateral plate element based on sampling surfaces method for 3D stress analysis, *Internat. J. Numer. Methods Engrg.* 108 (1) (2016) 26–54.
- [40] T.H.H. Pian, K. Sumihara, Rational approach for assumed stress finite elements, *Internat. J. Numer. Methods Engrg.* 20 (9) (1984) 1685–1695.
- [41] T.H.H. Pian, State-of-the-art development of hybrid/mixed finite element method, *Finite Elements Anal. Des.* 21 (1–2) (1995) 5–20.
- [42] E.A. de Souza Neto, Y.T. Feng, On the determination of the path direction for arc-length methods in the presence of bifurcations and ‘snap-backs’, *Comput. Methods Appl. Mech. Engrg.* 179 (1–2) (1999) 81–89.
- [43] S.P. Timoshenko, J.M. Gere, *Theory of Elastic Stability*, Courier Corporation, 2009.
- [44] J.C. Simo, D.D. Fox, M.S. Rifai, On a stress resultant geometrically exact shell model. Part II: The linear theory; computational aspects, *Comput. Methods Appl. Mech. Engrg.* 73 (1) (1989) 53–92.
- [45] J.C. Simo, M.S. Rifai, D.D. Fox, On a stress resultant geometrically exact shell model. Part IV: Variable thickness shells with through-the-thickness stretching, *Comput. Methods Appl. Mech. Engrg.* 81 (1) (1990) 91–126.
- [46] F.W. Williams, An approach to the non-linear behaviour of the members of a rigid jointed plane framework with finite deflections, *Quart. J. Mech. Appl. Math.* 17 (4) (1964) 451–469.
- [47] R.D. Wood, O.C. Zienkiewicz, Geometrically nonlinear finite element analysis of beams, frames, arches and axisymmetric shells, *Comput. Struct.* 7 (6) (1977) 725–735.
- [48] G.M. Kulikov, S.V. Plotnikova, Non-linear strain–displacement equations exactly representing large rigid-body motions. Part II. Enhanced finite element technique, *Comput. Methods Appl. Mech. Engrg.* 195 (19–22) (2006) 2209–2230.
- [49] R.H. MacNeal, R.L. Harder, A proposed standard set of problems to test finite element accuracy, *Finite Elem. Anal. Des.* 1 (1985) 3–20.
- [50] M. Bohlooly, S.V. Plotnikova, M.A. Kouchakzadeh, G.M. Kulikov, Three dimensional stress analysis of plates using assumed natural strain method and sampling surfaces method applied to the four-node quadrilateral plate element, *Adv. Mater. Technol.* 4 (3) (2019) 41–49.
- [51] K.J. Bathe, *Finite Element Procedures*, Prentice-Hall, New Jersey, 1996.
- [52] K.J. Bathe, A. Iosilevich, D. Chapelle, An inf-sup test for shell finite elements, *Comput. Struct.* 75 (2000) 439–456.
- [53] E.M. Campello, P.M. Pimenta, P. Wriggers, A triangular finite shell element based on a fully nonlinear shell formulation, *Comput. Mech.* 31 (6) (2003) 505–518.
- [54] J.C. Simo, D.D. Fox, M.S. Rifai, On a stress resultant geometrically exact shell model. Part III: Computational aspects of the nonlinear theory, *Comput. Methods Appl. Mech. Engrg.* 79 (1) (1990) 21–70.
- [55] P. Wriggers, F. Gruttmann, Thin shells with finite rotations formulated in biot stresses: Theory and finite element formulation, *Internat. J. Numer. Methods Engrg.* 36 (12) (1993) 2049–2071.
- [56] ANSYS 2019 R2 Release, ANSYS Inc, Canonsburg, PA, 2019.
- [57] F. Fallah, M.K. Vahidipoor, A. Nosier, Post-buckling behavior of functionally graded circular plates under asymmetric transverse and in-plane loadings, *Compos. Struct.* 125 (2015) 477–488.
- [58] J.H. Argyris, H. Balmer, J.S. Doltsinis, P.C. Dunne, M. Haase, M. Kleiber, G.A. Malejannakis, H.P. Mlejnek, M. Müller, D.W. Scharpf, Finite element method—the natural approach, *Comput. Methods Appl. Mech. Engrg.* 17–18 (1) (1979) 1–106.
- [59] J.C. Simo, L. Vu-Quoc, A three-dimensional finite-strain rod model. Part II: Computational aspects, *Comput. Methods Appl. Mech. Engrg.* 58 (1) (1986) 79–116.
- [60] M. Ritto-Corrêa, D. Camotim, On the arc-length and other quadratic control methods: Established, less known and new implementation procedures, *Comput. Struct.* 86 (11–12) (2008) 1353–1368.